Agricultural Water Management 316 (2025) 109584

Contents lists available at ScienceDirect

Agricultural Water Management

journal homepage: www.elsevier.com/locate/agwat

A process-based modelling of groundwater recharge under contrasting irrigation methods in semi-arid crops

Taha Attou [a,b,*], Sylvain Kuppel [b], Mohamed Hakim Kharrou [a], Jamal Ezzahar [c,d], Lhoussaine Bouchaou [a,e], Yassine Ait Brahim [a], Valérie Demarez [f], Abdelghani Chehbouni [c,f]

[a] *International Water Research Institute, Mohammed VI Polytechnic University, Benguerir 43150, Morocco*
[b] *Géosciences Environnement Toulouse, Université de Toulouse / CNRS / IRD / CNES, Toulouse, France*
[c] *Center for Remote Sensing Applications, Mohammed VI Polytechnic University, Benguerir 43150, Morocco*
[d] *Département IRT, Laboratoire MISCOM, Ecole Nationale des Sciences Appliquées, Université Cadi Ayyad, Morocco*
[e] *Laboratory of Applied Geology and Geo-Environment, Faculty of Science, Ibn Zohr University, Agadir 80000, Morocco*
[f] *Université de Toulouse/IRD/CNRS/CNES/CESBIO, Toulouse, France*

ARTICLE INFO

Handling Editor - Dr Z Xiying

Keywords:
Irrigation efficiency
Groundwater recharge
Ecohydrological modelling
Multi-objective calibration
EcH2O

ABSTRACT

We present an application of the process-based ecohydrological model EcH$_2$O to evaluate water-energy coupling and resulting percolation beneath the root zone under contrasting irrigation practices in a semi-arid region. The study uses high-resolution data from two wheat fields employing flood and drip irrigation, in a multi-objective calibration and evaluation approach with datasets encompassing soil water content at two depth ranges, energy balance components, and percolation rates at two depths. We find that the model reasonably simulates water fluxes and energy partitioning, and captures the distinct hydrological responses of the different irrigation methods. The best overall performances were found at both sites using calibration scenarios combining all available datasets, pointing at complementary information footprints. These footprints were nonetheless heterogeneous, as for example simulation of energy balance components showed little change between calibration scenarios, while percolation fluxes were acceptably captured only if the corresponding datasets were included in the calibration. Results highlight larger percolation dynamics and amounts beneath the root zone of flood-irrigated wheat, yet the two indices used here for irrigation efficiency reveal opposite rankings between the two irrigation methods depending on whether deep percolation is included (as a proxy for aquifer recharge) or not in the hydrological system being analysed. These findings challenge the view on greater water-saving benefits associated with drip irrigation, given the complex trade-offs between irrigation amounts and timing, plant water use, and return flows (e.g. underlying aquifer recharge). This analysis is a step forward for informing integrative and sustainable water management strategies in arid and semi-arid agricultural contexts.

1. Introduction

Water resources in arid and semi-arid regions are inherently limited and will continue to be a significant challenge in the future (Hargrove et al., 2023), due to the combined impact of climate change and the substantial increase in water demand for urban areas, industry and agriculture (Kharrou et al., 2021, Kundzewicz. 2008, Cai. 2015, Jounaid et al., 2020). Irrigated agriculture is by far the dominant driver of freshwater consumption, and irrigated areas are projected to increase, especially in North Africa (McDermid et al., 2023). In Morocco, irrigated agriculture occupies only 15 % of cultivated land surface but consumes 87 % of national water resources, generates about 45 % of agricultural Gross Domestic Product and 75 % of agricultural exports (Global Yield Cap Atlas, 2022). This hydrological footprint constitutes one of the main challenges for a sustainable Moroccan agriculture sector in the 21st century, leading to urgent consideration of improved water management strategies. Increased pressure on groundwater resources in Morocco may partly result from recent ambitious agricultural policies (e.g., the Green Morocco Plan launched in 2008, and the green generation program 2020–2030), these strategies promote modern "excessively intensive" agricultural models that place additional strain on water resources (Akesbi, 2014, World Bank, 2020). The agricultural

---

* Corresponding author at: International Water Research Institute, Mohammed VI Polytechnic University, Benguerir 43150, Morocco.
E-mail addresses: taha.attou@um6p.ma, taha.attou.th@gmail.com (T. Attou).

https://doi.org/10.1016/j.agwat.2025.109584
Received 28 December 2024; Received in revised form 13 May 2025; Accepted 28 May 2025

sector in a number of regions in Morocco has subsidised the reconversion of flood irrigation systems to more efficient irrigation technologies over the last twenty years, particularly drip irrigation.

The amount of water saved as a result of these programs, on the other hand, has rarely been quantified (Benouniche et al., 2014). This knowledge gap calls for a careful examination of the efficacy of these change in irrigation practices in terms of water resource conservation, in the face of the oft-observed "irrigation efficiency paradox": plot- or farm-level gains in irrigation efficiency seldom reduce water consumption at larger scales (Grafton et al., 2018). This negative outcome arises either because the "saved" portion at farm scale (from increased efficiency) is often water that previously recovered through aquifer recharge or runoff for downstream reuse, because of a switch to more water-intensive crops, or because of an increase of the irrigated crop area (Ward and Pulido-Velazquez, 2008). In Morocco's Souss and Tensift basins where the studied Haouz region is located (see Sect 2.1), subsidised conversion to drip irrigation has been shown to increase overall water consumption due to inadequate practices, increased crop transpiration and/or unreduced soil evaporation, and/or cropping intensification and expansion (with a growing share of tree plantation) (Molle and Tanouti, 2017). These structural issues further put at risk underlying aquifers through over-withdrawal and thus groundwater depletion, which can also cause land subsidence (Bouchaou et al., 2008) and water quality issues (Ez-zaouy et al., 2022, Mansir et al., 2021).

Groundwater recharge occurs when infiltration and percolation exceeds evapotranspiration (ET) and continues to flow downward through the vadose zone toward the water table, replenishing the aquifer (Jasechko et al., 2014). In arid and semi-arid regions where potential evapotranspiration frequently exceeds precipitation, recharge is generally a small component of the annual water balance, making it crucial to accurately quantify percolation rates beneath the root zone and therefore recharge (Ouarani et al., 2023). Among the numerous methods for quantifying ET and recharge fluxes, integrated numerical models that couple a process-based energy balance solving with subsurface hydrology and plant phenology (e.g., Tague et al., 2004, Ivanov et al., 2008, Fatichi et al., 2012, Maneta and Silverman, 2013, Niu et al., 2014, Bao et al., 2017, Kuffour et al., 2020) offer the possibility to disentangle the various components and dynamics of the water budget, including soil evaporation and root water uptake in relation to percolation patterns. This ability for process coupling and predictive power is advantageous in the changing high-energy hydroclimatic and land cover conditions often characterising semi-arid areas, as compared to modelling approaches with a more empirical calculation of ET components based on potential evaporation in such semi-arid crops (e.g., Toumi et al., 2016, Er-Raki et al., 2021, Abou Ali et al., 2023, Ourrai et al., 2024).

However, this flexibility with an increasingly-detailed integration of physically-based descriptions comes at the price of an increased need of input forcings (e.g. climate fields and topography) and a large number of parameters related to the different subdomains of the model (vegetation, surface, subsurface, aquifer, etc.). Such an issue of process and/or parameter identifiability can be addressed by jointly calibrating and evaluating simulations with different types of ecohydrological observations in a approach, thus leveraging several types of information content in a diversity of ecohydrological datasets to constrain different groups of modeled processes (Clark et al., 2011, Fatichi et al., 2016). This multi-objective model-data fusion approach can result in degraded performance (Fenicia et al., 2008, Scudeler et al., 2016) and poorer predictive power (Cao et al., 2006) if the different constraints "pull" the model in opposite directions (Clark and Vrugt, 2006, Efstratiadis and Koutsoyiannis, 2010), if the model misses key processes (Beven, 2006, McDonnell et al., 2007), or if there is a significant discrepancy of scales between data and simulation outputs (Piovano et al., 2018). However, many applications of multi-criteria calibrations using hydrological models reported clear benefits with increased number of diagnostics and performance across processes (Clark et al., 2011, Birkel et al., 2014, Kuppel et al., 2018a, Piovano et al., 2018, Seibert and McDonnell, 2002).

In this study, we build on such a successful multi-objective application (Kuppel et al., 2018a, Douinot et al., 2019, Ackerer et al., 2023) to evaluate how a process-based model-data approach with ecohydrological datasets can enhance the robustness of water and energy partitioning quantification and eventually assessing the impact of irrigation practices on the water recharge patterns. To this end, we use the process-based model EcH_2O (Maneta and Silverman, 2013, Kuppel et al., 2018a) for the first time in Morocco, in two types of irrigated wheat fields in arid agricultural lands. By constraining the model with several combinations of data types (soil moisture, energy balance components and percolation fluxes) from in situ monitoring over a growing season and notably analysing evapotranspiration and percolation fluxes, we test two hypotheses: (i) jointly calibrating with datasets of energy fluxes, soil moisture, and -where available- percolation is essential for accurately simulating both energy and water dynamics, and reduces the uncertainties associated with estimating groundwater recharge. (ii) Drip irrigation in winter wheat enhances water efficiency both from an agronomic (i.e. ET-oriented) standpoint as well as when jointly considering ET and percolation flow recharging the aquifer. The overall methodological flowchart is described in Fig. 1. Applying this methodology aims at paving the way for developing process-oriented, robust ecohydrological modelling framework to inform hydrologically-sustainable decision making in semi-arid agricultural contexts.

2. Materials and methods

2.1. Study sites

The Tensift basin is located in central Morocco, and characterised by climate ranging from arid in the Haouz plain with 150 mm of annual rainfall to humid continental climate in the Atlas mountains with annual rainfall exceeding 1000 $mm.yr^{-1}$ (Chehbouni et al., 2008). With an average annual potential evapotranspiration (PET) of 1600 $mm.yr^{-1}$ in the plain (Er-Raki et al., 2010), the evaporative demand is considerable. The region's surface and groundwater resources are being intensively exploited by agriculture and domestic uses, which are growing at a rapid pace in tandem with the region's economic development (Boukhari et al., 2015). Groundwater levels in the Tensift basin have been steadily declining since the 1980s as a result of these climatic and human-induced constraints (Le Page et al., 2012). The Tensift wadi's flow, which serves as a collector of surface water downstream of the Haouz plain, as well as the recharge of aquifers, are inextricably linked to the High Atlas's flows (Ouassanouan et al., 2022). A portion of the High Atlas runoff infiltrates into the wadi beds that lead to the piedmonts (Boukhari et al., 2015). Snowmelt and rainfall each contribute significantly different amounts of water to the hydrosystem's water balance.

The central Haouz's flow regime depends on the watersheds' rainfall and the High Atlas' melting snow. The reasonably dense hydrographic network of this area of Haouz runs from the High Atlas (N'Fis, Reghaya, Ourika, and Zat) to the Tensift river, which discharges into the Ocean. The Haouz has two sections. Watersheds on the southern side, contributing to output if the rivers water them and they get enough rain and snow. Haouz's plain, with extensive urbanization and agricultural activities, is considered as a consumption or transit zone.

The Haouz basin has two aquifer systems of varying importance in terms of underground water resources. The first concerns the deep Jurassic, Cretaceous, and Eocene reservoirs, which have low productivity, limited extension, and end in a few kilometers north of the Atlas (Moukhchane, 1983). The second reservoir is the Plio-Quaternary series, resulting from the atlasic chain breaking. This one has a free water table all over the plain, from 30 to 260 m deep. The region's most productive water table is also the most exploited. The extreme spatial variability of the hydraulic gradient reflects the structural complexity of these

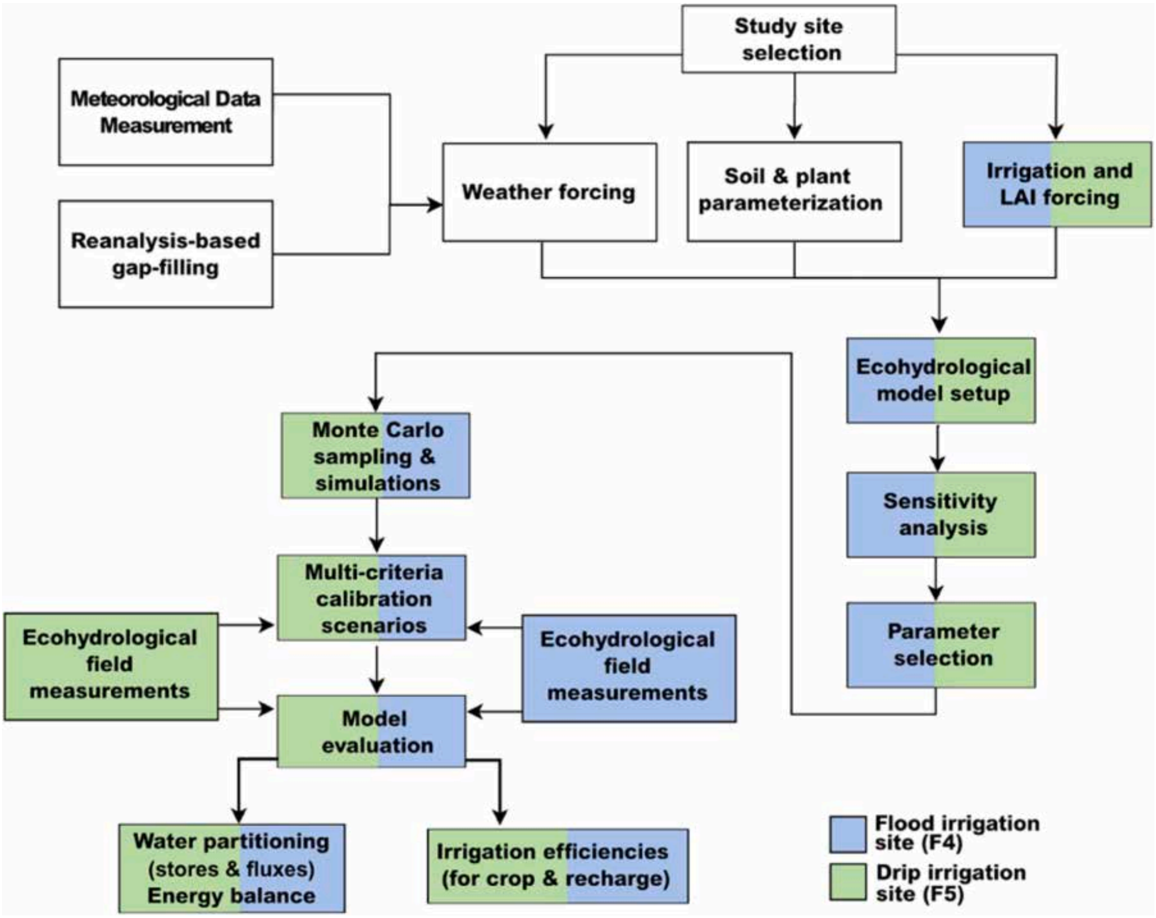

Fig. 1. Flowchart describing the methodology of the model-data approach used in this study, indicating the various and associated study sites.

deposits. These continental formations are highly variable in permeability. As one goes deeper, the permeability decreases as the facies become more clayey. The water table circulates in the Pliocene and Quaternary formations reworked by the Atlas wadis. The plain's silty cover limits vertical supply from rainwater or irrigation water infiltration. Groundwater in the region historically recharged through alluvial fans and wadis, with flow patterns directing water from the Atlas Mountains toward the Oued Tensift, Oued Tessaout, and Oued Gano gaps in the Jebilets. However, recent studies reveal a significant shift, indicating that the Tensift River no longer receives base flow from the aquifer, resulting in perennial dry conditions (El Mezouary et al., 2024). Additionally, the khettaras, once a critical component of traditional water management and irrigation systems, have ceased functioning, and no groundwater outlets or resurgences currently reach the Tensift wadi in the north.

This hydrological imbalance is further exacerbated by continuous groundwater overexploitation and the absence of sufficient recharge, leading to persistent and severe depletion of the water table. Groundwater extraction is now predominantly achieved through hand wells and mechanical pumping, contributing to the accelerated decline of aquifer levels and increasing pressure on remaining resources.

The experiment was conducted during 2015–2016 growing season over two wheat fields within the irrigated perimeter known as R3 in the Haouz plain (Fig. 1), which is located approximately 45 Km east of Marrakech (31.6341224 N, −7.63333 E). F4 field covers 4 ha of flood irrigated wheat, whereas F5 field covers 2 ha of drip irrigated wheat. Both sites were characterised by a clay soil texture consisting of 47 % clay, 35 % silt, and 18 % sand. The sowing dates for wheat were December 22nd and December 13th of 2015, for F4 and F5 respectively. The volumes of irrigation that were applied at each flood irrigation event for field F4 were 512 millimetres spread into 8 irrigation events of 64 mm, while at field F5 the total applied irrigation amount was lower (354 mm) and with more variable amount per events, ranging between 15 and 46 mm (Fig. 2 and Table S1).

2.2. *Data description*

The datasets utilised in this work were acquired from two experiments conducted during the investigated 2015/2016 agricultural season. Meteorological data were measured very close to both study plots. The weather station was equipped with standard automated sensors that measure incoming solar radiation, air temperature and humidity, vapor pressure, wind velocity, and precipitation. Each study plot was equipped with a set of sensors to measure: (i) the four components of the net radiation (Rn) using a CNR4 radiometer (Kipp & Zonen); (ii) the soil heat flux (G) at different depths using heat flux plates (HFT3-L, Campbell Scientific Ltd.); (iii) the surface temperature using IRTS-P's (Apogee); (iv) the soil temperature at different depths using (temperature probe 108). Beside these measurements, two eddy covariance systems were installed at each field to provide continuous measurements of sensible (H) and latent heat (LE) fluxes at height of 2 m. This system consisted of a 3D sonic anemometer (CSAT3, Campbell Scientific Ltd) and a fast hygrometer (KH20, Campbell Scientific Inc., USA). Raw data were sampled at a rate of 20 Hz and were recorded using CR3000 data loggers (Campbell Scientific Ltd.). The half-hourly fluxes were later calculated off-line using post-processing software package ECpack. To assess the quality of EC measurements, the surface energy balance closure test is commonly used. The analysis of the linear regression forced through the origin of the sum of sensible and latent heat fluxes against the available energy (Rn - G) yielded slopes of 0.71 and 0.70, with correlation

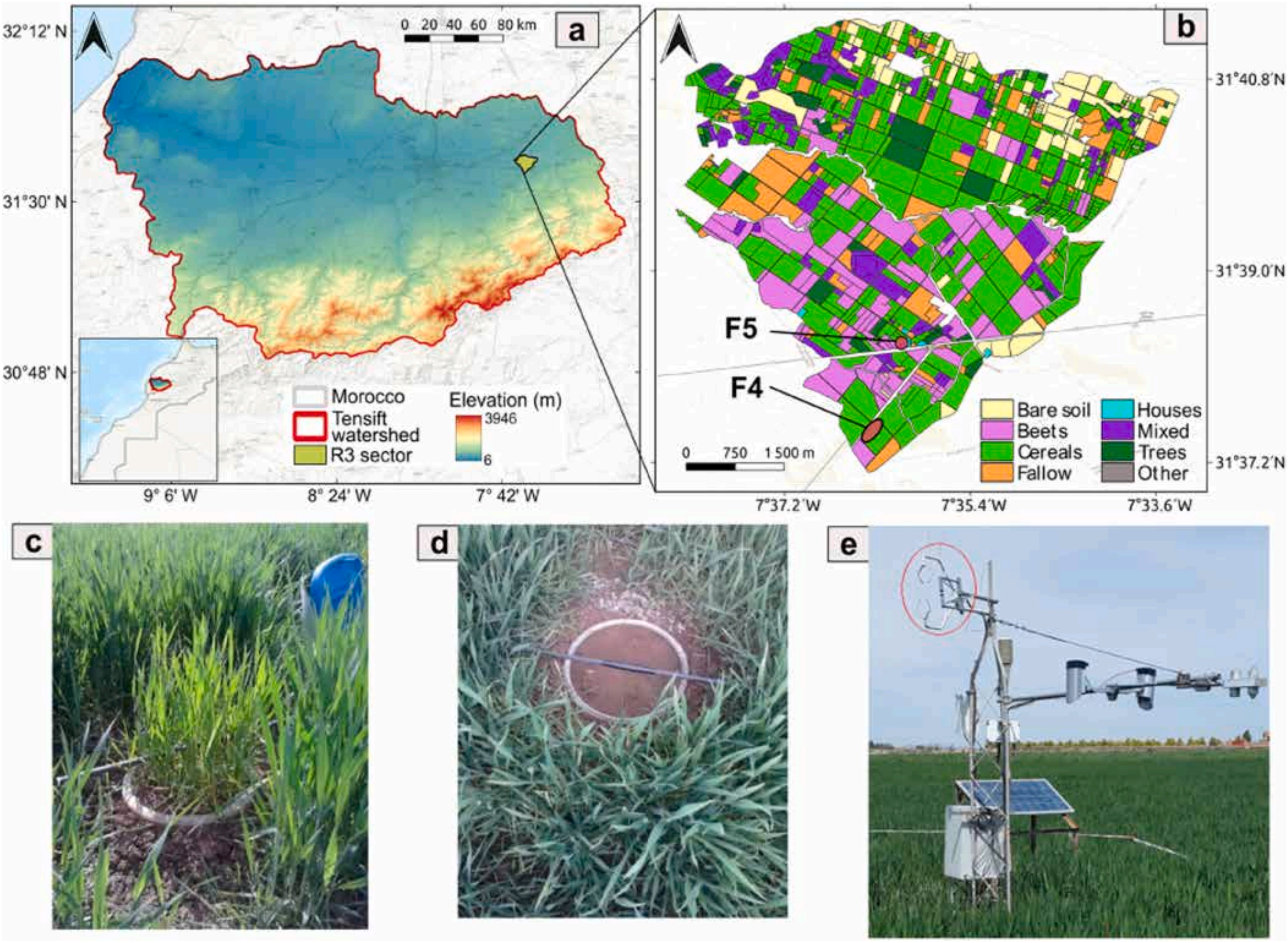

Fig. 2. Location of the Tensift watershed in Morocco (a), with a further detailed map of the R3 agricultural sector (b) showing land use and the location of the monitored plots F4 and F5 where the instruments are installed, including the small lysimeters in covered wheat (c) and bare soil (d) at F5 plot, and one of the two eddy-covariance systems (e).

coefficients of 0.94 and 0.92 for fields 4 and 5, respectively. Compared to findings from other experimental studies, where energy balance closure errors typically range from 10 % to 30 % (Twine et al., 2000), the closure achieved in this study can be considered acceptable.

The soil water content in both fields F4 and F5 was measured using a Time Domain Reflectometry (TDR) device (CS616, Campbell Scientific Ltd.) at various depths (5, 10, 20, 30, 40, and 50 cm). TDR measurements were recorded at a frequency of 1 Hz and saved as averages every 30 minutes using CR23X data loggers from Campbell Scientific Ltd. Similarly, the TDR readings were calibrated by doing weekly gravimetric measurements of soil water content at various depths. Based on these depth-specific measurements, for each time step a vertically-integrated values, corresponding to the depth of the model layers (see Sections 2.3 and 2.4), were used for model calibration and evaluation (sect. 2.5).

In addition to the aforementioned measures, two small lysimeters (METER Smart Field Lysimeter) with a diameter of 30 cm were placed on the F5 field. These lysimeters, with a depth of 30 cm and 90 cm, were used to measure the actual drainage. Both devices use a highly sensitive load cell positioned beneath the soil column to measure the amount of water that collects or evaporates from the leaves or soil surface with a high resolution. Another high-precision load cell is positioned beneath the drainage bottle to precisely weigh the water that exits the root zone through drainage. The 90-cm depth lysimeter was installed on the same date when the wheat field was sown whereas the 30-cm depth lysimeter was left under bare soil conditions, while the surrounding area remained undisturbed to replicate the environment of the wheat field. To reflect the irrigation system conditions, a single dripper supplied water to the soil surface above the lysimeter cylinder. Both lysimeters are equipped with tension control mechanisms, enabling the measurement of water flows at the subsurface (30 cm) and at the bottom (90 cm). No measurements were made on F4 site, as the experiment focused on assessing the efficiency of the drip irrigation technology, which has been largely adopted by farmers, thanks to the government's financial support in the frame of the MGP ("Morocco Green Plan"), particularly over wheat, one of the main crops cultivated in the studied region. Finally, the hemispherical canopy photos (taken with a Nikon Coolpix 950 and an FC-E8 fish-eye lens converter, field of view 183°) and the metric method were used every week to measure leaf area index (LAI) over each field along the growing season 2015–2016 (Fig. 3).

2.3. *Ecohydrological model*

The spatially distributed, process-based ecohydrological model EcH$_2$O couples a two-layer (canopy and understory) vertical energy balance scheme (Fig. 5a), a hydrologic module resolving vertical and lateral water transfers (Fig. 5b), and a transpiration-based simulator of carbon uptake and allocation for plant growth in order to simulate the energy and water dynamics in the soil-plant-atmosphere continuum (Lozano-Parra et al., 2014, Maneta and Silverman, 2013). EcH$_2$O has

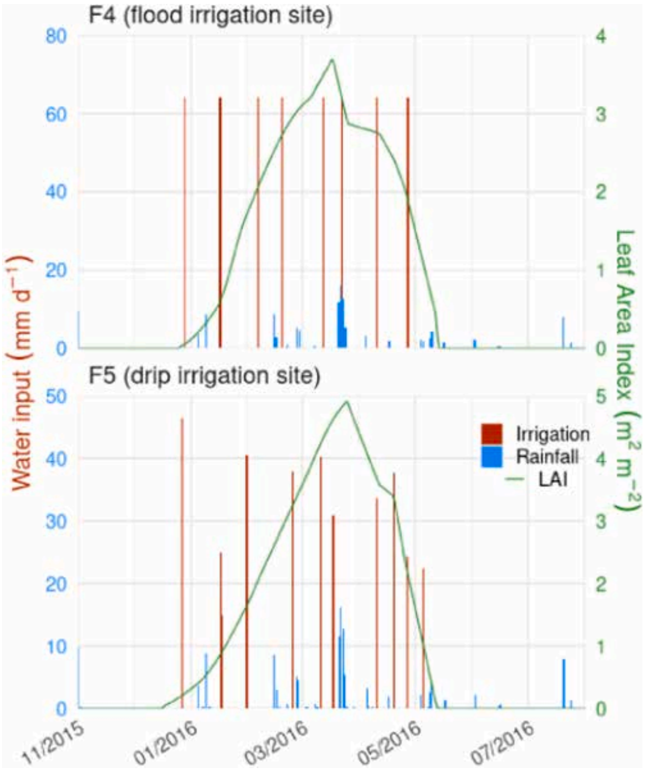

Fig. 3. Time series of water inputs (precipitation in blue and irrigation events in red) and crop phenology (leaf area index, green) from October 2015 to October 2016 at the two study sites: flood irrigation plot (F4, top) and drip irrigation (F5 plot, bottom).

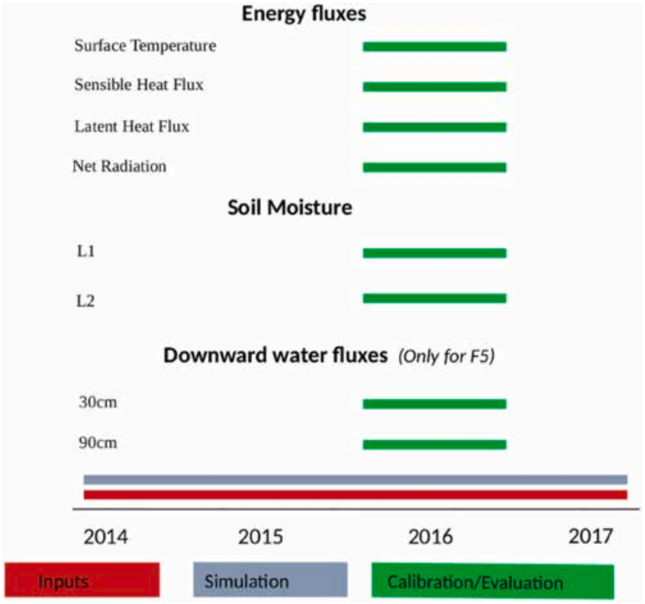

Fig. 4. Time periods spanned by the datasets available at the two sites F4 and F5, used to feed model inputs (red) over the simulation period (grey) and for model calibration/evaluation (green).

been primarily employed in forested ecosystems (Maneta and Silverman, 2013, Kuppel et al., 2018a) but also agricultural settings (e.g., Yang et al., 2021, Ackerer et al., 2023, Luo et al., 2024), along spatial scales typically ranging from 1–100 m^2 plots (e.g., Douinot et al., 2019, Li et al., 2023) to basins of 1–100 km2 (e.g., Neill et al., 2021, Yang et al., 2023, Maneta and Silverman, 2013). Our study provides a plot-scale application of this model to solve water flows for the first time in a semi-arid irrigated agricultural region.

The primary elements of the water balance in the vertical soil-vegetation column consist of canopy interception reservoir, the surface layer and three soil layers (Fig. 5a). Interception of precipitation inputs follows a linear bucket approach, where precipitation exceeding the maximum storage capacity makes up throughfall. For this application, the model was modified to account for irrigation, which is treated as a separate forcing input directly bypassing interception. The Green and Ampt approach (Mays, 2010) is used for surface water infiltration to the top soil layer, while downwards water percolation to deeper layers mobilises soil moisture exceeding field capacity; in all cases using a hydraulic conductivity linearly increasing with the degree of soil saturation using the Brooks and Corey approximation of pedotransfer functions (see Appendix of Kuppel et al. 2018a for further details). The leakage at the bottom of the simulated domain, which is here analysed as feeding groundwater recharge beneath the root zone (see the geometry described in Section 2.4) follows the same routing approach modulated by a dimensionless leakance parameter (Maneta and Silverman, 2013). Lateral and channel water routing is not described here, as the model is used in 1D with a no-flow lateral condition and without a stream network.

At each time step, the energy balance is solved at the canopy and surface levels using radiation inputs and separately calculates the rates of evaporated plant interception, of soil evaporation, and of plant transpiration in tight connection with the available water in the interception reservoir, in the first soil layer, and in the three soil layers (weighted by the root fraction), respectively. These evaporative losses are also controlled by the seasonal changes in LAI as it notably determines canopy conductance, light interception, and maximum canopy storage capacity. Instead of using the carbon allocation module to dynamically calculate the vegetation state (Lozano-Parra et al., 2014, Maneta and Silverman, 2013), following Ackerer et al. (2023) we take LAI as an external forcing from observations, which enables to control the water demand from foliar dynamics driven by anthropogenic activities in the two agricultural plots studied here.

2.4. *Simulation setup*

The model simulations were performed at an hourly time step from January 2014 to December 2017 over a 1-ha, one-pixel spatial domain. The first 12 months were discarded as a spin-up, to remove transient impacts of initial conditions of water content. The depth of the first hydrological layer, where soil evaporation occurs, was set to 10 cm, while the bottom of the second model layer was set to 30 cm in order to directly compare simulated downward water fluxes with the data collected from the lysimetric plate at this depth at the F5 site. Similarly, the total depth of the simulated domain (i.e. bottom of the third hydrological layer) was fixed to 90 cm, where the second lysimeter plate is situated, while also encompassing the bulk root zone beneath which water percolation feeds aquifer recharge.

Hourly meteorological inputs were primarily taken from the local weather station datasets for rainfall, incoming short-wave radiation, air temperature, wind speed, and relative humidity. Incoming long-wave radiation time series, not routinely measured for the local weather station, were taken from the ERA5-Land hourly climate reanalysis data (Muñoz-Sabater et al., 2021), which also served for filling in situ meteorological data gaps. Irrigation timing and amount were taken for each site (F4 - flood irrigation and F5 - drip irrigation) from the 2015/2016 growing season (Section 2.2 and Table S1), assuming the daily-scale amount for each event was evenly spread over 6 hours at F4 starting from 10:00 (typical values averaging the variability of the mutualised flood irrigation system), while at F5 an average irrigation rate of 6.25 mm/hour was used to spread to daily amount on a hourly basis starting at 8:00 when farmers usually switch on the drip system;

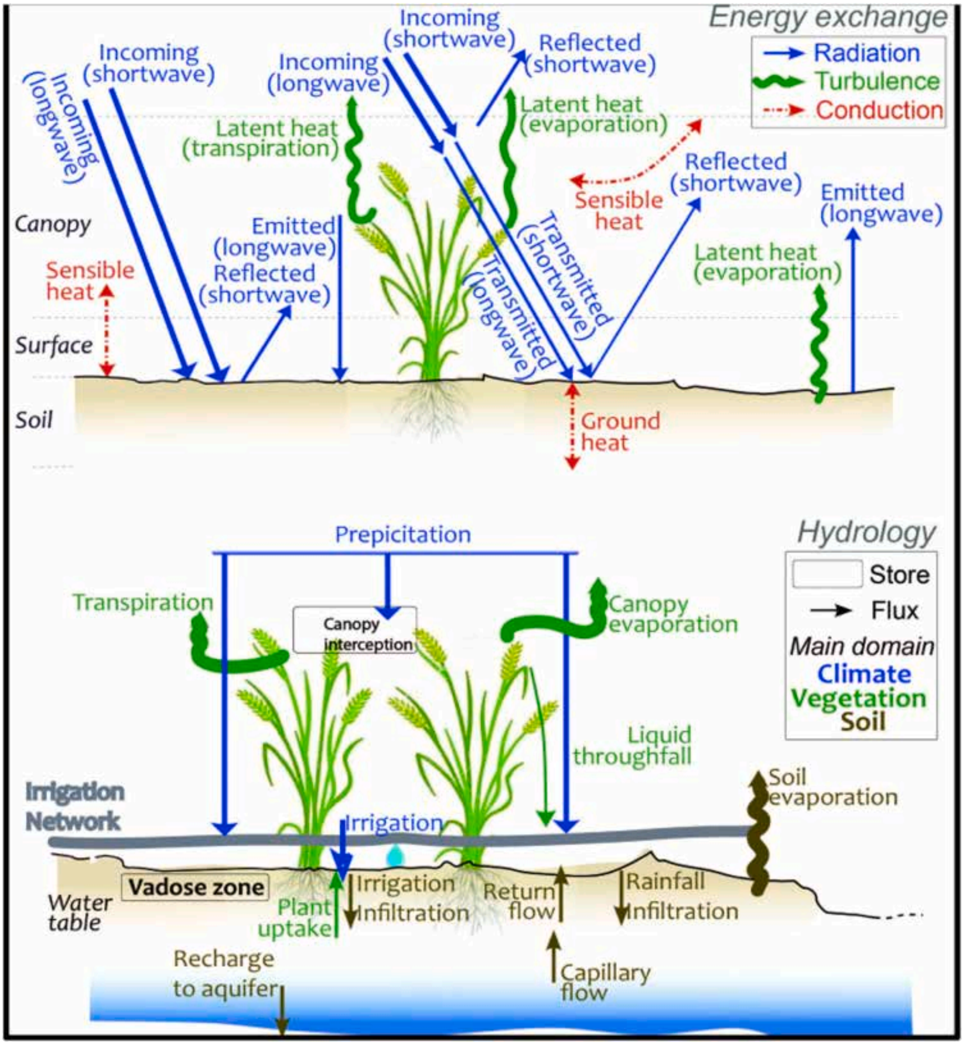

Fig. 5. Schematic representation of the fluxes and stores taken into account in the formulation of the EcH$_2$O model regarding transfers of (a) energy and (b) water.

this forcing was then replicated over the other simulated years. Similarly, LAI measurements, made over 2015–2016 at each site (see sect. 2.2), were used as inputs replicated over all simulated years. For model evaluation (see sect. 2.5), modelled surface temperature above the canopy is taken as an average between soil surface temperature and canopy surface temperatures computed during surface- and canopy-level energy balance solving, respectively, weighted using the canopy fraction available along with LAI measurements.

2.5. Sensitivity analysis, calibration and evaluation strategy

A preliminary sensitivity analysis was conducted to identify the parameters to include in the subsequent model calibration. We used the modified version of the Morris method (Morris, 1991) outlined in Sohier et al. (2014), which consists in changing parameter values one at a time (by half of each parameter's sampling interval, see Sohier et al., 2014) and quantifying the resulting difference in model outputs, here using the root mean square error (RMSE), yielding an "elementary effect" when divided by the parameter variation. This procedure was repeated over 20 trajectories following the radial points approach with initial parameter values sampled using a Latin Hypercube Sampling (LHS) design to maximise parameter space coverage, and the final elementary effect for each parameter on each model output of interest is taken a the average of the absolute elementary effect in each trajectory, often called μ^* (Sohier et al., 2014), thus given as:

$$\mu_k^* = \frac{1}{N_{traj}}\sum_{i=1}^{N_{traj}}\left|\frac{RMSE\left(M\left(X_1^i,\ldots,X_{k-1}^i,X_k^i+\Delta X_k,X_{k+1}^i,\ldots,X_n^i\right),M\left(X^i\right)\right)}{\Delta X_k}\right|, \tag{1}$$

where X is the vector of model parameters values, k is the index of the parameter to be tested, M is the time series of a given model outputs, X_k^i is the initial value of the k-th parameter in the i-th trajectory, ΔX_k is the variation of the parameter k, and N_{traj} is the number of trajectories used. In order to be able to compare elementary effects across parameters and outputs with ranges and units, we normalised parameter variation by its allowed range (yielding a variation $\widetilde{\Delta X_k}$of ± 0.5, see above) and we also normalised each type of model outputs by their 80 %-dispersion range across all sensitivity simulations. We applied this method to the 25 parameters related to hydrodynamic properties, soil physics and vegetation functioning, and considering as relevant model outputs those used during calibration: soil moisture at two levels, latent heat, sensible heat, net radiation, and (only for F5 site) downwards percolation fluxes at two depths (see also calibration description below). Finally, we selected the parameters that showed a median normalised elementary effect across outputs equal or larger than 10 % for at least one the two sites. It allowed us to select 13 parameters for model calibration, mostly related to soil hydrodynamics properties and vegetation hydrological functioning (Table 1).

The EcH$_2$O model was calibrated using a Monte-Carlo multicriteria

Table 1
Main numerical parameters used in the simulations, displaying fixed values and ranges used for calibration. *: log-sampling.

Name	Description	Unit	Calibration range
Subsurface			
ϕ	Total porosity	$m^3.m^{-3}$	0.3 – 0.5
K_{hsat}	Saturated horizontal hydraulic conductivity	$m.s^{-1}$	$1e^{-7}$ – $8e^{-6}$ [*]
k_{leak}	Leakance parameter	-	0.001 – 1 [*]
λ_{bc}	Pore size distribution parameter	-	2 – 12
Ψ_{ae}	Air entry pressure head in the soil	m	0.05 – 0.8
Vegetation			
gs_{max}	Maximal stomatal conductance	$m.s^{-1}$	0.005 – 0.025
T_{opt}	Optimal photosynthesis temperature	°C	15 – 30
K_{beer}	Light attenuation coefficient	-	0.4 – 0.7
CWS_{max}	Maximum interception storage capacity	$m.LAI^{-1}$	$5e^{-5}$ – $5e^{-4}$
gs_{vpd}	Sensitivity of stomatal conductance to vapour pressure deficit	Pa^{-1}	0.0001 – 0.003 [*]
Ψ_{low}	Soil water potential for complete stomatal closure	m	150 – 250
Ψ_{high}	Soil water potential removing hydrological control on stomatal conductance	m	3.5 – 80
k_{root}	Shape coefficient for exponential root profile	m^{-1}	0.4 – 10 [*]

approach where the performance of a large ensemble of sampled model parameterizations is ranked based on the combined distributions of various model-data goodness-of-fit (GOFs) across several outputs, rather than combining the cross-outputs GOF values themselves (Ala-Aho et al., 2017, Kuppel et al., 2018a). The steps are as follows: 1) 88 000 sets of 13 parameters were generated using a latin hypercube sampling with uniform distributions within the calibration ranges listed in Table 1; 2) each set was used for individual runs at F4 and F5, where various model-data GOFs were quantified for each run using a model performance metric (see below); 3) the cumulative distribution functions (CDFs) of site- and output-specific GOFs were determined; 4) individual rankings were combined for each multi-criteria calibration scenario (see Table 2) by determining the quantile value above which exactly 30 "best runs" simultaneously maximise rankings for each associated GOFs. These calibration scenarios were developed to combine the diversity of constraints by grouping into process related to water storage (soil water content at 0–10 cm and 10–30 cm), downward water transfer (percolation at 30 cm and 90 cm depths) and energy balance (sensible heat, latent heat, and net radiation). The performance metric used for calibration is the Kling-Gupta Efficiency (KGE, Gupta et al., 2009), which defines an Euclidian distance (ED) from an ideal point, here of perfect model-data agreement, to be minimized:

$$ED = \sqrt{(\alpha - 1)^2 + (\beta - 1)^2 + (r - 1)^2}, \tag{2}$$

$$KGE = 1 - ED, \tag{3}$$

where β is the ratio between the mean of simulations and observations, α is the ratio between the standard deviations of simulations and observations, and r is the linear correlation factor between simulations and observations. KGE is thus to be maximized, with a variation range from -∞ to 1, and a KGE value above -0.41 indicates that simulations are a better predictor than the mean of observations (Knoben et al., 2019). Note that we did not use calibration metrics based on squared model-data difference, such as the Nash-Sutcliffe efficiency (NSE) and RMSE, because they are known to overemphasize the constraint brought by high-values and neglects low-value portions of the dataset (e.g. Krause et al., 2005). In our case, several of the measurements types we use for calibration, such as energy balance fluxes and downward percolation fluxes, have non-symmetrical distribution, especially at the hourly time scales where the calibration is done. KGE comparatively offers a more balanced "weighting" of model-data fit during calibration, which combines criteria for bias, correlation. Given the short time period available for calibration datasets (one growing season), the calibration period was not separated from the evaluation period. Our evaluation of model performance then focuses on cross-output propagation of information content (instead of propagation of model performance from calibration to evaluation period) by analysing how the model performs for output included or not in the 8 calibration scenarios considered across the two study sites. Here we use dimensionless GOFs to evaluate the model across outputs types: KGE, to which we added the RMSE normalised by the mean of observations as a fraction-type metrics (taking into account the limitations discussed above).

Table 2
Description of the different calibration scenarios used at the two study sites F4 and F5.

Site	Scenario	Constraint	Metrics
F4	F4_SWC	Soil water content in two upper layers (0−10 cm, 10−30 cm)	KGE
F4	F4_EB	Energy balance components: latent heat, sensible heat and net radiation fluxes	KGE
F4	F4_SWC_EB	Soil water content in two upper soil layer and energy balance fluxes	KGE
F5	F5_SWC	Soil water content in two upper layers (0−10 cm and 10−30 cm)	KGE
F5	F5_EB	Energy balance components: latent heat, sensible heat and net radiation fluxes	KGE
F5	F5_SWC_EB	Soil water content in two upper layers and energy balance fluxes	KGE
F5	F5_Prc	Downward water fluxes at 30 cm and 90 cm depths	KGE
F5	F5_SWC_EB_Prc	Soil water content, energy balance fluxes and downward water fluxes	KGE

Finally, the dispersion across ensemble runs is quantified using a normalised predictive uncertainty (PU*) defined as the 80 % spread of each simulated daily value across the 30 "best runs" of a given calibration scenario averaged over the whole simulation period, excluding the initial spin-up phase:

$$PU^{*} = \frac{1}{N_{eval}} \sum_{i=1}^{N_{eval}} \frac{M_{90}(t_i) - M_{10}(t_i)}{\langle |M(t_i)| \rangle} \tag{4}$$

where $M_{90}(ti)$, $M_{10}(ti)$, and $\langle |M(ti)| \rangle i$ are respectively the 90th percentile, the 10th-percentile and average absolute value for the i-th time step in the calibration period.

3. Results

The following subsections are organised to present the model-data patterns in time series and seasonal fluxes (sect 3.1), then the overall model performance and dispersion between calibration scenarios (sect 3.2), and finally relate these analyses to the calibrated values of model parameters (sect 3.3). While the numerical simulations of the different variables were conducted and the model parameters were calibrated on a hourly time step basis, for visual clarity we display the results using daily averages for the simulated time series (Figs. 6–8), the corresponding performance metrics (Fig. 9) and predictive uncertainty (Fig. 10).

3.1. Time series of ecohydrological observables

Fig. 6 shows that the model is able to capture most of the soil moisture dynamics down to 30 cm, for most calibration scenarios at both sites. At the flood irrigation site (F4), all scenarios are able to capture the timing of the response to the 6 irrigation events covered by the datasets (Fig. 6, left panel). The calibration scenarios including soil moisture data (F4_SWC and F4_SWC_EB) unsurprisingly provide a better

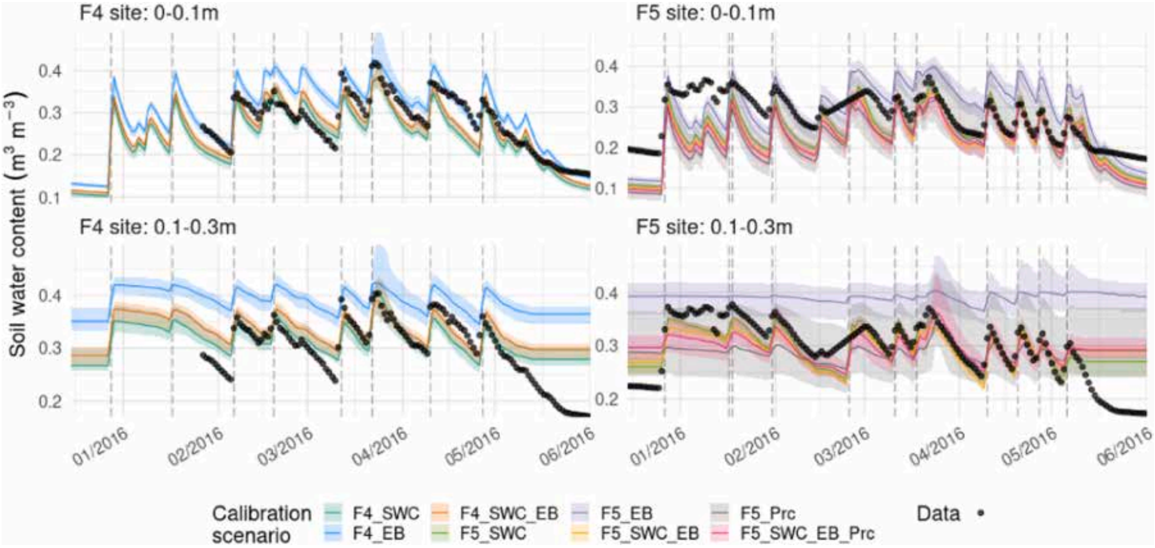

Fig. 6. Time series of daily-averaged soil volumetric water at the F4 (left) and F5 (right) sites over the 2015–2016 growing season, for the two uppermost layers of the simulated domain: 0–10 cm (top), and 10–30 cm (bottom). Data points (black) overlay the median and 80 % dispersion interval of the ensemble simulations for each calibration scenario (colours, see Table 2 for details). Vertical dashed lines represent irrigation events.

performances than when only radiation components are used for calibration (F4_EB); this difference is most marked in the deeper soil layer (10–30 cm) where F4_EB simulations overestimates (ensemble-median biases of $+0.03\ m^3.m^{-3}$ at 0–10 cm and $+0.09\ m^3.m^{-3}$ at 10–30 cm) and slightly dampens soil moisture dynamics. The misfit of the "radiation-only" scenario is even more marked at the F5 site (F5_EB) and visible in both layers where biases are similar to F4 ($+0.01\ m^3.m^{-3}$ at 0–10 cm and $+0.09\ m^3.m^{-3}$ at 10–30 cm) more overdamped signals (Fig. 6, right panel). The scenarios combining several types of constraints but including soil moisture (F4_SWC_EB, F5_SWC_EB, and F5_SWC_EB_Prc) yield similarly good results as compared to those using soil moisture alone, yet sometimes with an increased dispersion across best runs. This ensemble dispersion is even larger when only using water percolation data as constraint (F5_Prc), but with a good overall capture of observed SWC values at both depths. None of the scenarios seem to be able to fully catch the decrease of soil water content measured at both F4 or F5 sites in the deeper layer (10–30 cm) at the end of the growing season.

Fig. 7 compares the simulated and observed components of the surface energy balance: latent heat flux (LE), sensible heat flux (H), net radiation flux (Rn) and surface temperature (Ts). The calibrated model configurations overall capture the seasonal dynamics over the 2015–2016 growing season at both sites, with very similar results between calibration scenarios. Latent heat flux displays the best model-data agreement, as simulations manage to capture the seasonal increases and short term dynamics of LE from January to May 2016 at both sites (overall ensemble-median biases lower than $4\ W.m^{-2}$ across scenarios); only the decrease at the end of the growing season is overestimated by the model at both sites. This good performance is thus reflected in the simulation of actual evapotranspiration (ET), well reproduced both in terms of range and seasonal dynamics at both sites (Fig. 8), with higher modeled and measured ET rates at the flood irrigation plot F4 as compared to drip irrigation plot F5. Most calibration scenarios nonetheless result in overestimating some peak ET rates at the beginning of the growing season following irrigation events at both F4 and F5 sites, yet at the latter site this overestimation seems more significant and persistent until mid-March 2016, and we note an overall bias on order of magnitude larger at F5 (-0.8 to $+0.7\ mm\ d^{-1}$) than at F4 (-0.04 to $0.09\ mm.d^{-1}$). Including energy balance constraints at the F4 site (F4_EB and F4_SWC_EB) results in realistically lowering some of these ET peaks. The overestimated LE decrease before the harvest in Spring 2016 simulations is also found for ET underestimation at F4 site, while late-season ET simulations remain in good agreement with observations at F5 site. At the F5 site, we also note that the energy-balance-driven scenario (F5_EB) notably degrades the ET fit, which is underestimated from mid-February until the harvest period.

At both sites, consistent biases were observed in the simulation of the other energy balance components, despite reasonably-reproduced dynamics at both seasonal and submonthly timescales. The sensible heat flux is somewhat overestimated in simulations with an overall ensemble-median bias of 13 to $25\ W.m^{-2}$ across scenarios; the largest misfit is generally at F4, but also at F5 before February 2016 when leaves and plants start to grow (see LAI in Fig. 3). Surface temperature showed an even larger discrepancy, with a model overestimation of 6 to 6.5°C overall, most visible in the late growing season. Furthermore, net radiation is well reproduced at F5 for most of the growing season, but the model underestimates this flux before February 2016 at this site (median bias of -25 to $-29\ W.m^{-2}$), while at F4 site a larger bias is found throughout the analysed period (-42 to $46\ W.m^{-2}$). Additionally, the F5_Prc scenario results in some overestimated peaks late March 2016 for latent heat, sensible heat and surface temperature, when net radiation is conversely underestimated by F5_Prc simulations.

Fig. 9 reports the downward water fluxes at 30 cm depth (top) and 90 cm depth (bottom, corresponding to groundwater recharge) under the two different sites and thus irrigation methods, mostly showing simulations but also the lysimeter-observed values available at F5 site for part of the growing season. At the F4 plot where flood irrigation is used, the infiltration peaks closely follow irrigation events. The infiltration fluxes reach 18 to 68 mm/day at a depth of 30 cm on irrigation days and return to a no-flow condition within 2 days, with almost no intra-scenarios dispersion and little difference between calibration scenarios. More differences are visible at 90 cm depth, with scenarios F4_EB and F4_SWC_EB displaying more intense percolation events (with ensemble-median values up to $14\ mm\ d^{-1}$) concentrated over 72 hours following the irrigation events, while simulations calibrated using only soil water content data (F4_SWC) report a more dampened response to irrigation events with smaller peak percolation rates (ensemble-median values up to 5 mm/day) with a recession spanning several days up to 2 weeks.

In the F5 plot managed with drip irrigation, percolation fluxes are more numerous but less intense as compared to the F4 site, with marked differences between calibration scenarios at both 30 cm and 90 cm depths. Quick and intense responses to irrigation events are simulated at

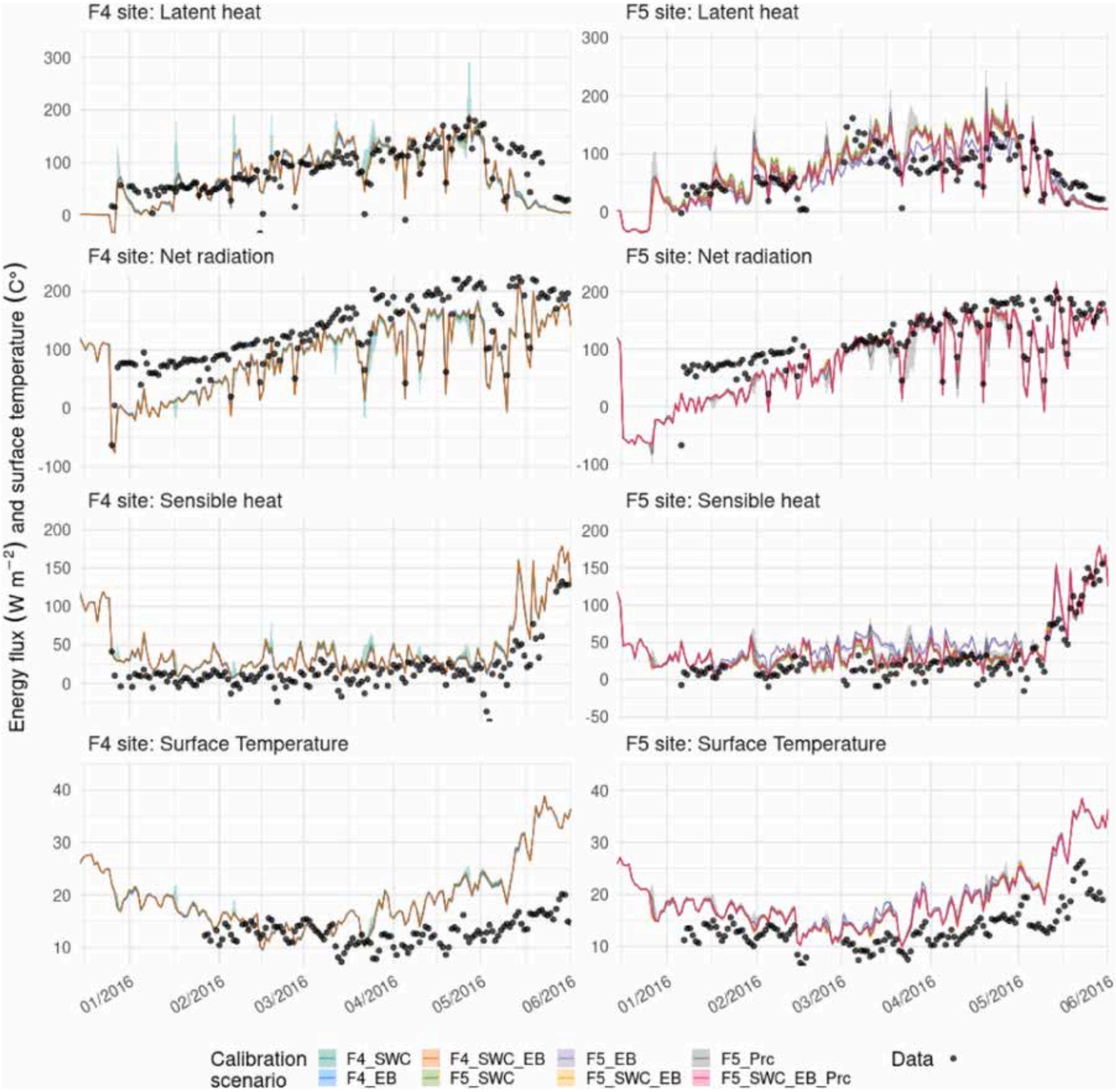

Fig. 7. Time series of daily-averaged observed and simulated latent heat, net radiation, sensible heat surface temperature at F4 (left) and F5 (right) sites over the 2015–2016 growing season, with observations displayed in black and simulations (80 % dispersion range and average of best runs) shown with colours.

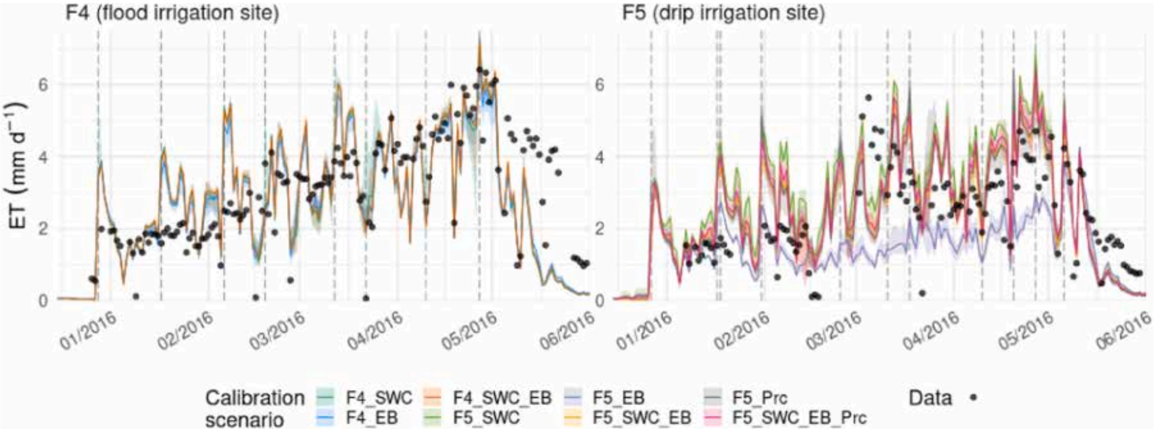

Fig. 8. Time series of observed and simulated daily-averaged evapotranspiration rates at F4 (left) and F5 (right) sites over the 2015–2016 growing season, with observed data displayed in black and simulations with colours (80 % dispersion and median of best runs) for each calibration scenario. Vertical dashed lines represent irrigation events.

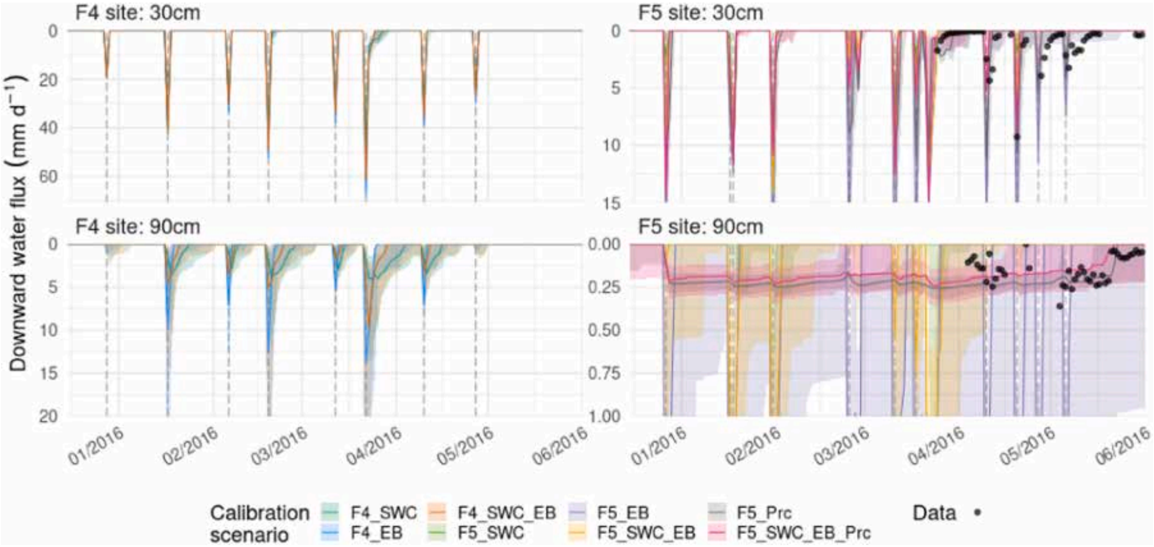

Fig. 9. Time series of downward water fluxes at F4 (left) and F5 sites (right) over the 2015–2016 growing season, showing daily-accumulated percolation rates at depth 30 cm (top) and 90 cm (bottom, corresponding to groundwater recharge). Observations at F5 are shown in black, while the median and 80 %-dispersion of ensemble simulations are shown with colours corresponding to each calibration scenario. Vertical dashed lines represent irrigation events. For clarity, the y-axis is capped at 15 and 1 mm d^{-1} at 30 cm and 90 cm for F5, respectively (right), hiding percolation peaks in some scenarios (up to 67 and 17 mm d^{-1} at 30 cm and 90 cm, respectively).

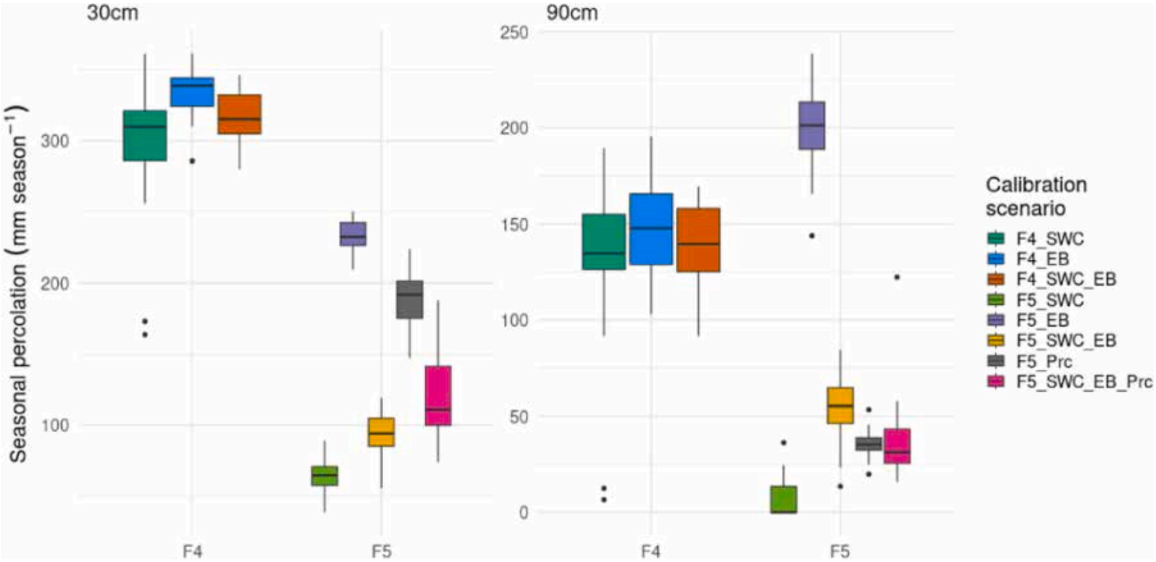

Fig. 10. Simulated cumulative estimates of downward water fluxes across the growing season (Dec 2015 - June 2016) at 30 cm (left) and 90 cm (right), with box plots depicting the distribution of values for the two sites and associated calibration scenarios.

30 cm for all calibration scenarios, although the largest peak infiltration values (up to 33 mm d^{-1} for ensemble-median, beyond the y-axis of Fig. 9 top-right) were found when lysimeter data was not used (F5_SWC, F5_EB, F5_SWC_EB). This order of magnitude is larger than the typical range given by the available lysimeter data from April to May 2016, which reach up to 9 mm d^{-1} at 30 cm depth, although data gaps prevent a comprehensive comparison with the modelled peaks outside the end of the growing season (April-May). At this depth, F5_Prc simulations comparatively remained in better agreement with the lysimeter data in terms of dynamics and range, while also being the only scenario with F5_EB to simulate percolation at 30 cm following the 2 latest irrigation events of the season. At the 90 cm level, all scenarios display more dampened percolation dynamics than at 30 cm, yet with significant contrasts between calibration scenarios. Those not using lysimeter data as constraint (F5_SWC, F5_EB and F5_SWC_EB) display one or several percolation events concentrated over a few days with values (up to 15 mm d^{-1}) much beyond the typical range reported by the available lysimeter data (~0.4 mm d^{-1}), and F5_SWC and F5_SWC_EB fail to simulate percolation after late March 2016 although observations indicate downward water fluxes at the end of the growing season. By contrast, simulations calibrated using lysimeter data information (F5_Prc and F5_SWC_EB_Prc) display flatter variations without no-flow periods consistent with lysimeter data available at the end of the growing season, noting that the scenario F5_Prc allows to better capture the observed recession following percolation in May 2016.

The cumulative percolation fluxes reflect the differences reported between sites and across scenarios (Fig. 10). Simulations at the flood irrigated plot (F4) yields seasonal percolation amounts almost one order of magnitude larger than in the drip irrigated plot (F5) in most cases, both at 30 cm and 90 cm depths. At the F4 site, all scenarios yield a seasonal 30 cm infiltration within a 290–352 mm range (0.1–0.9 IQ range over scenarios), while percolation below the root zone (90 cm) is within a 109–181 mm range with the lower values obtained with the F4_SWC scenario. At the F5 site, the scenarios including soil water content data resulted in lower seasonal percolation at 30 cm (51 to 164 mm) while other scenarios yield values 2 to 3 times higher. At 90 cm where estimates may approximate below-root recharge, the F5_EB scenario yields much higher values (177–225 mm range) than the all other scenarios (including at the F4 site), with F5_SWC yielding a no-flow median estimate and the apparently-similar range for the 3 remaining scenarios within a 18–78 mm range hides drastically different short-term dynamics (Fig. 9).

3.2. *Overall model performance and predictive uncertainty*

The model performances are summarised in Fig. 11, where heat maps relate calibration scenarios using two model-data GOFs (KGE and root mean square error normalised by the mean of observations - RMSE*) for each of the evaluated output variables whose time series are shown in Figs. 6–9, including a cross-observable average in each case; Fig. 11 displays ensemble-median values. At the F4 site, most of the evaluated outputs display good performance ($0.2 < \text{KGE} < 0.8$) with small KGE variations (< 0.2) between calibration scenarios, with two notable exceptions: the sensible heat flux with KGE values around -0.55 and RMSE* values around 1.5 across scenarios and surface temperature (see below). The former model-data discrepancy is not found for simulations at F5 site which is more consistent with higher KGE values (0.18 to 0.56) and lower RMSE* values (< 1) reported in Fig. 11. Normalised RMSE values at F4 site otherwise inversely reflect KGE patterns, with the lower values found for topsoil water content in the ($\text{RMSE}^* < 0.2$ and $\text{KGE} > 0.7$) while most simulated components of the energy balance (LE, Rn) and ET display RMSE* below 0.45. Interestingly, at F4 site the surface temperature display moderate RMSE* (≤ 0.7) despite poor KGE values (< -1), and modelled water content at 10–30 cm display low RMSE* values on par with topsoil moisture values despite medium-to-good KGE (0.23 to 0.44) suggesting a likely impact of comparatively poorer correlation factors.

The situation is more contrasted at the F5 plot, with larger ranges of KGE and normalised RMSE between scenarios and observables. Topsoil water content, latent heat fluxes, evapotranspiration, and net radiation simulations display high model-data agreement across calibration scenarios as seen from KGE values (and to a lesser extent through RMSE* values). A cross-scenarios consistency is visible for the poorer performance of surface temperature simulations ($0.14 \leq \text{KGE} \leq 0.18$, $0.51 \leq \text{RMSE}^* \leq 0.53$). Simulated percolation at both 30 cm and 90 cm consistently shows poor model-data fit with mostly negative KGE values beyond -0.1 and RMSE* mostly above 1 whenever lysimeter data is absent from the calibration (F5_SWC, F5_EB and F5_SWC_EB); including this information significantly improves median model-data fit at both depths from a KGE standpoint ($-0.21 \leq \text{KGE} \leq 0.14$), while RMSE* reduction is limited to simulation of percolation at 90 cm. We also note that the simulation of water content at 10–30 cm is significantly improved by including soil moisture data (F5_SWC, F5_SWC_EB, F5_SWC_EB_Prc) both in terms of KGE and RMSE*, as is (to a lesser extent) the simulation of ET, LE, H.

Overall, at both F4 and F5 sites, the scenarios including all considered calibration constraints yield the highest cross-observable median KGE values of 0.24 for F4_SWC_EB and 0.35 for F5_SWC_EB_Prc. The same ranking appears when considering RMSE* at F4 (0.52) and F5 (0.58).

The relative predictive uncertainty (PU*) in Fig. 12 reports the influence of various calibration scenarios on the ensemble dispersion for each evaluated simulation output, following a similar layout as Fig. 11, except that percolation outputs at F4 are also reported. It shows that PU* values of percolation fluxes at 90 cm (0.2 to 2.8) are often one order of magnitude higher than other simulated fields (0.006 to 0.8), with relatively similar values between sites for soil water content but generally higher values at F5 for energy-related outputs. Regarding these energy balance components, we also find that their predictive uncertainties are lowest at F4 site when energy terms (H, LE, and Rn) are the very constraints used in the calibration (top panel: uncertainties of ET, H, LE, Rn and Ts -columns 3 to 7- for F4_EB scenarios $-$2nd row), with median values equal or below 0.12. This analysis also applies to F5 site for soil moisture, as scenarios including these datasets (F5_SWC, but also F5_SWC_EB and F5_SWC_EB_Prc) yields lower PU* values for SWC than other scenarios. It does not apply for energy balance at F5 where F5_EB yields larger PU* values for energy balance outputs, nor for water storage at F4 site as F4_EB scenarios often yields lower PU* values of volumetric water content (1st and 2nd columns) than F4_SWC scenarios, yet in the latter case this seems to stem from the higher mean SWC

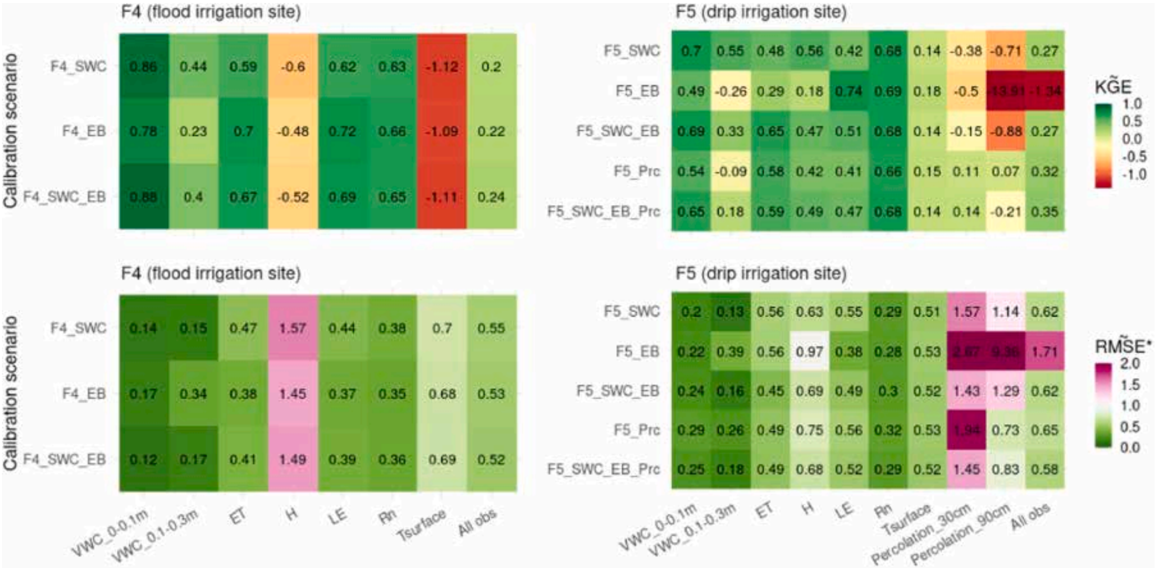

Fig. 11. Heat maps of model-data fit over the 2015–2016 time period at F4 (left) and F5 (rights) sites, as measured using the median daily-scale (top) KGE and (bottom) normalised RMSE over the ensemble runs for each of the calibration scenarios (rows) and each type of observation (columns), including an "all-observation" value.

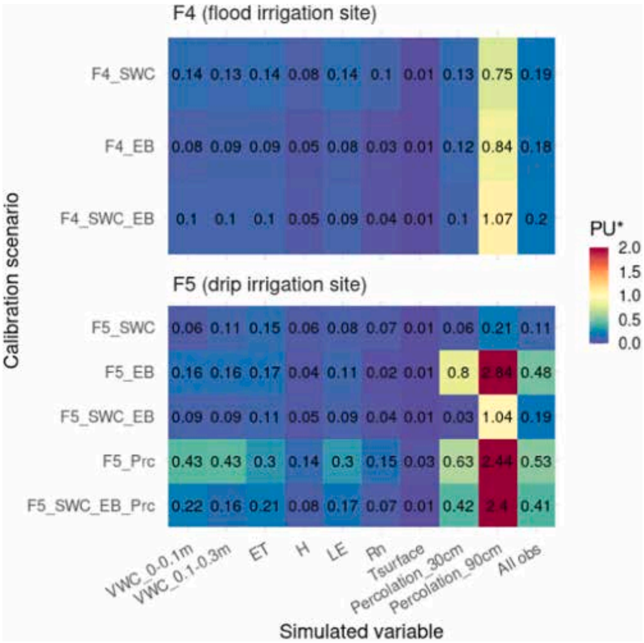

Fig. 12. Relative predictive uncertainty PU* at F4 (top) and F5 sites (bottom), computed for each simulation output (x-axis) as the daily-scale 80 %-range among the 30 ensemble runs for each calibration scenario (y-axis) best runs and then averaged over the 2015–2016 growing season.

values (with poorer model-data fit) reported in F4_EB scenarios (denominator of PU*) rather than a reduced absolute dispersion interval (Fig. 6). Regarding percolation fluxes, PU* values are generally much lower at 30 cm than at 90 cm, and there is a significant heterogeneity between calibration scenarios. Within each site, at 30 cm we find lower relative uncertainties for scenarios using SWC data at F5, while it is more ambiguous at F4. We also note that the "percolation-only" scenario at F5 (F5_Prc, 4th row in the lower panel of Fig. 12) yields the largest predictive uncertainty of all non-percolation outputs as compared to other calibration scenarios, but also yields large PU* for percolation at both depths. In the end, the best-performing scenarios (F4_SWC_EB and F5_SWC_EB_Prc) yields a similar predictive uncertainty as compared to most of the other scenarios at F4 while at F5 the comparatively large "All obs" PU* stems from that of 90 cm percolation (despite better model-data performance).

3.3. Parameter values

Fig. 13 shows the selected parameter values across the selected 30 best runs for each of the calibration scenarios jointly explored at both study sites. We first find that the calibrated values for hydrodynamic properties (total porosity ϕ, saturated hydraulic conductivity K_{hsat}, pore-size distribution coefficient λ_{bc}, and air-entry pressure head Ψ_{ae}) most often exhibit well-constrained values across different calibration scenarios as compared to the a priori sampling intervals (dashed horizontal lines in Fig. 13). The *a posteriori* values for these parameters are often consistent with the clayey nature of the soil at the study sites as grouped in Clapp and Hornberger (1978), with λ_{bc} values near or above 6 (higher values found at F4 site), Ψ_{ae} values between 0.5 and 0.7 m, and low hydraulic conductivity K_{hsat} (below 3.5e^{-6} m s^{-1}) yet with calibrated values at F4 generally higher (1.9 to 3.2e^{-6} m s^{-1}) than at F5 (2e^{-7} to 3.5e^{-6} m s^{-1}), a difference that holds when comparing "all-datasets" calibration scenarios (F4_SWC_EB and F5_SWC_EB_Prc). Total porosity (ϕ) values are somewhat more variable between scenarios, where calibrating using the radiation dataset only (F4_EB and F5_EB) yields larger values in a narrow range (0.48 to 0.49 m^3 m^{-3}) while other scenarios yield lower retention capacity (0.42–0.46 m^3 m^{-3}) except for the F5_Prc scenarios where total porosity is even lower with a larger dispersion across best runs (0.33 to 0.4 m^3 m^{-3}). We also observe that the *a posteriori* distributions for the leakance coefficient at the bottom (90 cm depth) of the simulation domain (k_{leak}) reports highest values for F4_EB, F4_SWC_EB, F5_SWC, F5_EB and F5_SWC_EB scenarios, combined with the more homogeneous distribution of K_{hsat} described above, explains the larger peak percolation rates observed at 90 cm for these scenarios at both sites (Fig. 9, bottom panels).

Vegetation parameters interestingly display some degree of clustering between sites, most visibly with light extinction coefficient (K_{beer}) and maximum stomatal conductance (gs_{max}) exhibiting higher values at F4 than at F5 site. This is also visible for the stomatal sensitivity to air dryness (gs_{vpd}) where the distinctly higher gs_{vpd} values at F5 (meaning more decline of stomatal conductance at higher VPD), combined with gs_{max} patterns above, are consistent with the higher ET rates simulated (and observed) at F4 than F5 (Fig. 8). Rooting depth calibration (through the k_{root} parameter) shows heterogeneous results, yet calibration scenarios using both soil water content and energy balance observations yield well-constrained values (i.e. with smaller *a posteriori* range in the log-sampled space) with shallower rooting depth (i.e. higher values k_{root}) at F5 than at F4: the F4_SWC_EB scenarios reports k_{root} values between 1.4 and 3.5 m^{-1} (corresponding to having 95 % of roots within 0.68 to 0.82 m), F5_SWC_EB reports k_{root} values from 7.5 to 9.6 m^{-1} (i.e., a 95 % rooting depth ranging from 0.31 to 0.40 m). Adding percolation data (F5_SWC_EB_Prc scenarios) slightly increases rooting depth at F5 to 0.33–0.43 m (with k_{root} values from 6.8 to 9.1 m^{-1}), noting that constraining the model only with percolation data (F5_Prc) yields much deeper rooting depth (>0.81 m). Other vegetation parameters, related to interception storage capacity (CWS_{max}), optimal photosynthesis temperature (T_{opt}), the range of soil water potential influence on stomatal conductance (from no control -Ψ_{high}- to stomatal closure -Ψ_{low}) comparatively show weaker patterns of calibrated values across scenarios.

4. Discussion

Process-based, integrative ecohydrological models bear significant potential for understanding and predicting dominant controls on water storage/release dynamics in the fast-evolving Anthropocene. However, their inherent high parameterization (since many processes are coupled/concatenated in related equations) make it challenging but crucial to leverage relevant information content yielding a reduced space of model configuration (i.e. diversity of parameter sets and/or of model structures) to eventually allow for process identification unambiguously (Clark et al., 2011). Multi-criteria calibration may help in that respect, with differentiated constraints among the various processes and parameters. Conversely, model-data discrepancies after calibration also offer opportunities to discuss and improve the model structure and model-data fusion strategy. In the present study, the overall good performances of multi-criteria calibration at two agricultural plots with contrasting irrigation practices allows such a discussion, focused below first on the analyses of identified (and missed) process dynamics, and then on the respective values of the combined information contents. Finally, we further discuss the potential and limitations of our methodology in the context of sustainable agricultural practices, using efficiency metrics.

4.1. Representation of biophysical processes

The best-captured output is soil moisture, here analysed down to 30 cm using two hydrological layers (0–10 cm and the 10–30 cm ranges), with the lowest cross-scenario RMSE* values and highest KGE compared to other fields. The time series in Fig. 6 further show that the EcH$_2$O model effectively captured the distinct patterns observed at the F4 and F5 sites throughout the agricultural season, resulting from the interplay of short-term responses to irrigation and rain events with

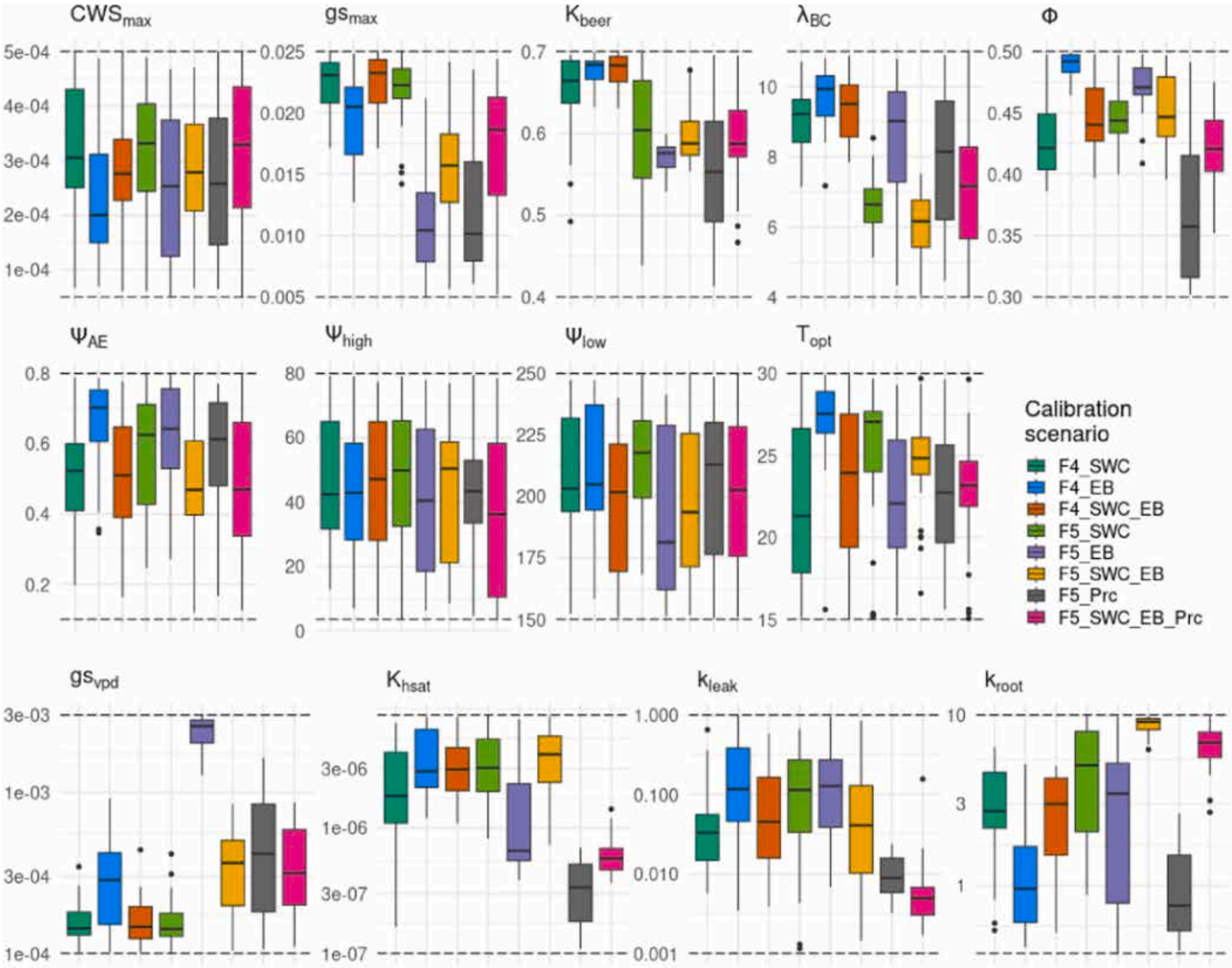

Fig. 13. A posteriori values of the 13 calibrated parameters, showing the distribution of values (interquartile range and median) across the 30 "best runs" for each calibration scenario at both sites (colours). A log-scale y-axis is used for the 4 parameters in the bottom row (log-sampled for calibration, see Table 1).

direct evaporation, shallow root water uptake, and percolation.

The time series however also highlights some limitations, first of all at F4 where the model is less dynamic than observations in terms of dry-down variability throughout the cropping season: in the topsoil layer (0–10 cm) dry-down dynamics are slightly overestimated (meaning that simulated VWC decreases too much) during the peak growing season (mid-March to late April) but well-captured before and after that, while in the intermediate soil layer (10–30 cm) dry-down dynamics are underestimated in early March and during the harvest period (early May), but well-simulated outside these periods (Fig. 6, left). While the magnitude and dynamics of total ET is overall correctly estimated across most of the cropping period (Fig. 8), an inspection of ET components (Fig. S1) shows that the overestimated ET peaks following irrigation events during the peak growing may derive from an overestimation of the relative contributions of soil evaporation plus root water uptake within the first 10 cm. These discrepancies in soil water content within the first 30 cm remain nonetheless quite small at F4 and point at a reasonable representation of root water uptake (RWU) along the full 90 cm profile.

At F5 site, the interplay between model-data fit for soil water content and ET is more contrasted. From mid-March until the harvest period when LAI declines (May), the excellent model-data fit of soil water content at both monitored depths ranges suggest an accurate balance between storage and water fluxes (ET and percolation components) when leaf cover is medium to high (see LAI in Fig. 3), noting that ET remains slightly overestimated. During the earlier growing stages until mid-March 2016, the joint inspection of overestimated dry-down dynamics at 0–10 cm in between well-capture peak moisture contents on irrigation days, overly responsive total ET and modelled ET components (Fig. S1), also points at an overly responsive contribution of soil evaporation. The slight underestimation of water content in the 10–30 cm depth range at that period further suggests that the model excessively evaporates topsoil water instead of percolating to deeper horizons as suggested in VWC data. The same early-season discrepancy in soil water content may be happening at F4 site where ET is also overestimated following irrigation events due to large rates of direct evaporation (Fig. S1), yet the absence of soil moisture data at that period limits our analysis.

Nonetheless, the recurrence of unreasonably large direct evaporation rates at both sites during early growing stages questions the quantification of available energy and/or available water for this ET component. When solving the surface energy balance, the whole storage in the upper model layer mobilized, i.e down to 10 cm; while this evaporation depth makes sense for clayey soils it represents a steady-state value for the evaporation front after several days or weeks (Wythers et al., 1999) following the different stages of direct soil evaporation (Or et al., 2013). As result, the simplified formulation of direct evaporation in the EcH$_2$O model may benefit from using a topsoil layer depth balancing between evaporation depths and resulting evaporation rates over the shorter times scales considered in the simulations, given the recurrence and timing of rain or irrigation events.

The calibrated rooting depth, down to 0.8 m for most F4 scenarios, is consistent with typically-reported values for flood-irrigated winter wheat (Kharrou et al., 2021). For the drip-irrigated plot (F5), calibration reports a shallower root system (within 40 cm for the best performing scenario F5_SWC_EB_Prc), which corresponds to the depth of maximum root activity found in these irrigation systems located in the middle and lower soil layers at the peak growing stages where drip irrigation increases root growth (Ma et al., 2022)]. Note that some of the above-described dynamics and discrepancies of (soil) ET may arise from the conceptualisation of RWU when solving the canopy-level energy balance to quantify transpiration. There, the relative weight of each of the three soil layers simulated by the EcH_2O model to plant-available water derives from a static root profile, embodied in the exponential shape parameter k_{root} (Kuppel et al., 2018a). This was originally developed for natural or semi-natural environments where it provided an adequate capture of RWU dynamics (Maneta and Silverman, 2013; Lozano-Parra et al., 2014; Kuppel et al., 2018a). As a result, it may lack the flexibility needed to reflect evolving RWU from the convolution of soil water status and root growth stages in crops, and most notably increasingly-deeper accessible soil horizons (Ma et al., 2022). Other simulation efforts in the same conditions such as Er-Raki et al., (2021) were also able to reproduce storage et evaporation dynamics despite using a fixed rooting depth of 50 cm with the HYDRUS-1D model (Šimůnek et al., 2008) under both irrigation systems.

The overall good capture of the broad hydrodynamic behavior along the soil profile in the F4 and F5 plots is also consistent with the calibrated parameters, whose values match the clay-rich texture of the soil at these study sites in terms of water retention capacity (medium-to-high index for pore size distribution, high air-entry pressure head and large total porosity) and low hydraulic conductivity (Fig. 13). We however note some differences between the two study sites, where the best-performing calibration scenario in the drip-irrigated plot yields lower water retention capacity (pore distribution and porosity) and lower hydraulic conductivity than the flood-irrigated plot despite similar soil properties (Er-Raki et al., 2021, Arjdal et al., 2024). Given that our modelling configuration takes into account the main differences between the two plots such as foliar dynamics (LAI signal) and irrigation timing and amplitude, we posit that these inter-site differences, as well as plant-level parametric differences such as consistently higher extinction coefficient, higher maximum stomatal conductance and lower VPD control of stomatal conductance at the flood irrigation site, could arise from parametric compensation due to using vertically-uniform hydrodynamic parameterization in inherently heterogeneous soil profiles. Our modelling approach indeed emphasized the coupling of physically-based canopy- and surface-level energy balance solving with a somewhat simplified subsurface hydrology to keep a high computational efficiency and thus allowing for in-depth exploration of parametric space through automatic calibration (see Sect. 4.2 as well). While it provided good overall results, it is at the expense of further exploring profile-level heterogeneity, and follow-up effort could use a layer-based parameterization and/or more calibration data such as direct measurements of field capacity could enhance the model’s accuracy without compromising the efficiency.

Beyond parameterization, the present modelling approach sought to explore the potential and limitations of using a simplified conceptualisation of vertical water movement through and within soil horizons. The EcH_2O model streamlines soil hydrology by utilising a layer-by-layer (saturated) gravitational flow, neglecting matric potential gradients, as opposed to more detailed (and computationally-intensive) descriptions such as the Richards-based HYDRUS-1D model used by Er-Raki et al. (2021). In addition, as in other 1D modelling approaches, the one-pixel domain used in this study laterally averages water storage and fluxes. Taken together, such simplifications are useful for utilising plot-scale datasets such eddy-covariance data, and leaf cover and meteorological forcings, but may hide smaller-scale processes like capillary effects and lateral redistribution, which are significant in fine-textured soils like those in the research plots (Pueyo et al., 2013). We also note some uncertainty regarding leaf area index time series used as an input. At F4 site, It is likely to explain the largely underestimated final dry-down at 10–30 cm at both sites in May 2016 (where simulations remain near field capacity near 0.3 m3 m-3) while it is well-captured at 0–10 cm; this is simultaneous with an underestimation of ET (Fig. 8, left) and an overestimation of surface temperature in the model (Fig. 7, bottom left), and the end of the decrease of LAI, from 1.5 (1 May) to 0 (13 May). A very similar pattern is observed at F5 where LAI recession is similarly timed, with a similar overestimation of surface temperature but a smaller misfit for ET and overestimated dry-down at 0–10 cm. The low-to-null LAI (and thus canopy fraction) values used to compute plot-level surface temperature (see sect. 2.4) may give a disproportionate weight to soil surface temperature which usually reach higher and less dampened values than canopy-level surface temperature, thus explaining the reported departures. We used the same leaf cover forcing as in Er-Raki et al. (2021), except for late growing season (after late March) where the cited study maintained a constant LAI (above 4) and canopy fraction (above 0.9) until early June, whereas it seems more realistic to stick to the original LAI dataset, which may conversely overestimate the LAI decline through April and May.

Finally, the present modelling approach was able to capture the range and the broad dynamics of percolation reported at 30 and 90 cm by the lysimeter data at the drip irrigation plot F5, with KGE above −0.4 (meaning that simulations performs better than the observation mean) at both depth for the overall best performing scenarios (F5_SWC_EB_Prc) only bested for this specific datasets by the percolation-only calibration scenarios (F5_Prc). Our estimates of cumulative percolation for these two scenarios at drip irrigation site (87–214 mm IQ range at 30 cm, 18–50 mm at 90 cm) are consistent with a previous process-based modelling effort estimating 93 mm at 50 cm depth (Er-Raki et al., 2021). At the flood irrigation site however, the HYDRUS-1D model used by Er-Raki et al. (2021) also yields similar yet thigher percolation flux at 50 cm (347 mm) than we report here at both depths with the reference F4_SWC_EB scenario (290–340 mm IQ range at 30 cm, 114–166 mm at 90 cm). The performances of this aforementioned study with more detailed hydrological conceptualization is quite uncertain given the discrepancy between measured and modelled percolation depth ranges. Directly comparing to available lysimeter data at the drip irrigation site, the present model-data fit is remarkable given the above-discussed limitations, and the small percolation rates at 90 cm (orders of magnitude smaller than percolation at 30 cm, ET and irrigation pulses) warranting precision for this “residual” percolation term. It emphasizes the paramount importance of an explicitly coupled energy balance - hydrology modelling scheme such as found in EcH_2O to explore the dynamic interactions between soil water status and plant - surface energy fluxes.

4.2. Tradeoffs and benefits of multi-observation model constraints

The study used numerous datasets in various combinations for model calibration and evaluation to provide new insights into the informativeness and representativeness of these measured quantities in enhancing our modelling methodology. This can aid in the development of more effective data collection initiatives.

From an energy balance perspective, we find that most of the components evaluated in this study (sensible heat, net radiation and surface temperature) are simulated similarly across the calibration scenarios within each site, with model-data fits ranging from fair-to-poor for surface temperature to good for net radiation, and with limited (but consistent) improvement from having energy balance observables included in the calibration (Fig. 11). The case is more significant for latent heat (used in some calibration scenarios) and related evapotranspiration (only used for evaluation) as both observables are well captured with all calibration scenarios in both study plots (median KGE > 0.5 in most cases), yet with noticeable improvements when energy balance (and sometimes soil water content) are included in the calibration (Fig. 11). An interesting case is the poor performance of evapotranspiration in the “energy-balance-only” scenario at F5 (F5_EB) despite consistent improvement for latent heat flux: despite solving the energy balance to compute the latter, the transpiration flux remains low (Fig. S1) due to a large sensitivity of stomatal conductance to air dryness for that scenario (embodied in the large value of gs_{VPD} parameter, Fig. 13), and the larger soil evaporation flux cannot compensate (Fig. S1). It illustrates the importance of including information content from water content along with energy balance to avoid overfitting of energy balance components at the expense of consistent ET partitioning and resulting degraded water content simulation (Fig. 6). The insufficient information content in the energy balance datasets is also visible at the F4 site, where the F4_EB scenario provides good results for these observables, but a degraded fit to soil water content (Fig. 6, left).

By contrast, the information provided by soil water content datasets alone already yields good performances for both soil water content dynamics -as expected- but also energy balance components (H, LE, Rn and Ts) both in the flood irrigation plot and in the drip irrigation plot. Combining with energy balance information in the calibration (in F*_SWC_EB scenarios) does bring some improvement to the simulation of the latter type of observables and does not significantly degrade simulations of soil water content (Fig. 11). This suggests that from an ecohydrological perspective the information content given by soil water content is broader (process-wise) than that given by the energy balance, at least at this plot scale (see also the discussion on the spatial footprint, e.g. in Kuppel et al., 2018a). Yet both these water and energy information contents remain “compatible” and complementary, notably enabling to identify narrower ranges of values for many parameters (see scenarios F*_SWC_EB in Fig. 13).

In the drip irrigation plot where lysimeter data at both the 30 cm and 90 cm depth allowed us to further calibrate and evaluate simulated percolation fluxes, we find that an acceptable model-data fit (outlined in Sect 4.1 as well) can be achieved provided that the calibration includes this specific dataset. At 30 cm depth where percolation dynamics are quickly responsive to irrigation events with measured rates reaching 10 mm/d, the model provided first-order agreement for a broader range of scenarios where soil water content and/or lysimeter datasets were included, although maximum rates may be overestimated. Good performing scenarios dwindle at the bottom of the simulated domain (90 cm) where the percolation flux is order of magnitude smaller than other vertical fluxes at differents horizons (ET, infiltration, percolation, irrigation); without lysimeter data, the model behaves similarly to the 30 cm horizon, resulting in overestimated dynamics and rates (Fig. 9, right). The most significant illustration of this discrepancy is the F5_EB scenario where this large overestimation of 90cm-percolation dynamics results in seasonally-sum flux even larger at the flood irrigation site (Fig. 10, right) and is associated with a very large predictive uncertainty (which almost covers the whole bottom right panel in Fig. 9). It highlights the limits of using energy balance constraints to estimate percolation since it primarily relates to surface and above-ground transfers with limited information content consistent with underground processes. Including only energy balance also tends to shift infiltrations rates and responsiveness up at the flood irrigation site, although the contrast with other scenarios combining water content and/or energy balance are much less pronounced than at the drip irrigation site, notably visible through seasonally-cumulative fluxes (Fig. 10). At this site where we noted a much higher baseline for percolation amounts and lower attenuation from 30 cm to 90 cm than at the drip irrigation site (Sect. 3.1), the larger predictive uncertainty at 90 cm than 30 cm (as also found for the drip irrigation site, Fig. 12) highlights the increased difficulty to predict downward water fluxes as one moves deeper along the soil profile.

Conversely, we also note that the information content of percolation datasets alone remains insufficient to effectively constrain soil water content simulations: the model-data fit is degraded at 10–30 cm (as compared to scenarios including SWC data) and the predictive uncertainty for SWC at both depths (0–10 cm and 10–30 cm) is 2 to 4 times higher than in other scenarios. This limited footprint of lysimeter data may however derive from the limited amount of data collected, which was only done on certain days (with numerous gaps) towards the end of the growing season, missing the majority of irrigation events and following recessions. This issue raises more generally the question of data quality and availability. Like any other process-based model in a calibration approach, the consistency from evaluation to process identification depends on the exhaustivity of constraining datasets.

In the end we find a more significant variability in model performance and/or estimates of unobserved fluxes across calibration scenarios at the drip irrigation site than at the flood irrigation site, but both sites converge in that using multiple data types bolsters the model’s robustness. It better captures distinct behaviors in flood (F4) and drip (F5) irrigation, linking soil moisture, energy fluxes, and percolation processes. For instance, F4_SWC_EB captures rapid infiltration under flood irrigation, while F5_SWC_EB_Prc reflects stable drip irrigation patterns. Extra constraints narrow parameter uncertainty and incorporating lysimeter data aligns recharge simulations more closely with reality. Ultimately, such integrated calibration reduces bias, avoids overfitting to single datasets, and is more likely to enhance predictive accuracy for unobserved conditions.

4.3. Implications for identifying efficient and sustainable irrigation practices with process-based modelling

Despite the limitations and remaining uncertainties of the modelling strategy adopted here that was discussed in the previous sections, the overall good model performances across a range of ecohydrological outputs allows for first-order assessments regarding the water budgets of the two irrigation types represented in the present study plots. In the following, we will mostly thus use the scenarios F4_SWC_EB and F5_SWC_EB_Prc as reference scenarios for further analysis, as they were found to be the most robust in terms of overall model-data fit and predictive uncertainty (see Figs. 11–12 and Sect. 3.4). The larger evapotranspiration rates found in the flood irrigation plot (F4), as compared to the drip irrigation plot (F5, Fig. 8), also reflect larger simulated transpiration rates (directly quantified by the EcH$_2$O model, see Sect 2.3); forward modelling with the reference calibration scenarios over the 2015–2016 cropping season (December to May) yields transpiration estimates ranging from 295 to 336 mm at F4 (0.1–0.9 IQ range across best runs) and 236 to 288 mm at F5 (not shown). To put this into an irrigation efficiency perspective, we divided the cropping-season transpiration by the total water input (precipitation + irrigation) over the same time period and for the abovementioned reference scenarios, yielding an *agronomic irrigation efficiency* (Fig. 14, left). We found slightly lower values at F4 (0.1–0.9 IQ range of 48–55 %) than at F5 site (52–63 %). In other words, our results of winter wheat water consumption suggest a larger efficiency of drip irrigation as compared to the flood irrigation plot studied here, from a pure agronomical standpoint. Further analysis including cropping yields would however allow for a more in-depth assessment of irrigation efficiency with a “pipe-to-harvest” perspective (Guo et al., 2023).

Considering that the backdrop of this modelling effort is to assess the sustainability of groundwater use practices, it is essential for hydrologically-based assessment of agricultural practices to also include deep percolation as a beneficial, “locally recoverable return flow” (Grafton et al., 2018) to the underlying aquifer, which precisely sustains groundwater resource either at the local scale (e.g. through pumping and thus the very irrigation inputs) or at the watershed scale for a range of hydrological functions. Taking advantage of the modelled percolation estimates at 90 cm (i.e. beneath the main root zone), we thus computed

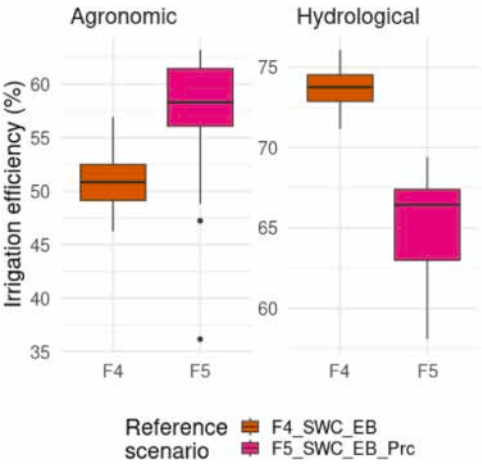

Fig. 14. Irrigation efficiencies, computed using transpiration (left) and transpiration plus deep percolation over the growing season (Dec 2015 - June 2016) with box plots depicting the distribution of values across reference calibration scenarios (see text for details).

another irrigation efficiency metric including both cropping-season transpiration and percolation amounts, here summed and divided by water inputs (precipitation and irrigation) over the same period, termed *hydrological irrigation efficiency*. Using the same reference calibration scenarios as above, we find that this efficiency is this time higher at the gravity plot F4 site (72–75 %, 0.1–0.9 IQ range) than at the drip irrigation site F5 (62–67 %, 0.1–0.9 IQ range) (Fig. 14, right). This estimate questions the oft-highlighted "water-saver" characteristic of drip irrigation over flood irrigation, as during the studied cropping season one third of incoming water did not sustain biomass production of drip-irrigated winter wheat or water recycling towards aquifer recharge, while this fraction is ~25 % for the flood irrigation system. Drip irrigation, while efficient at delivering water to the root zone and enhancing plant water use efficiency, is thus shown here to have a relative gain in productivity too marginal to compensate the reduced return flow to the hydrological system (percolation beneath the root zone) as compared to the flood irrigation system, while soil evaporation was not significantly reduced (with even an increased relative weight, from 22–24 % in F4_SWC_EB to 29–35 % in F5_SWC_EB_Prc, not shown).

These results may however be taken with caution, for several reasons. They are highly sensitive to the precision of our percolation estimates at both the drip irrigation site (10 to 100 times lower than other fluxes) and the flood irrigation site. For example, doubling the 90 cm percolation flux at the drip irrigation site (as compared to the reference F5_SWC_EB_Prc scenario) puts the hydrological efficiency on par with the flood irrigation, as does decreasing the percolation by 30 % at the flood irrigation site (as compared to the F4_SWC_EB scenario, not shown). It is not negligible given remaining uncertainties regarding local boundary conditions used for this modelling approach, such as the crop's leaf area index (LAI) or our assumption regarding irrigation timing. While we always started irrigation events at the same hour(for lack of more detailed information) and used average (although field-based) irrigation rates throughout the irrigation period, actual irrigation may be more variable due to factors such as labor availability, energy costs, and equipment constraints, and other non-physically-grounded human factors; this variability may also create temporary soil saturation or preferential flow paths influencing infiltration and percolation patterns. The latter feature is not accounted for in process-based modelling efforts so far (e.g. EcH_2O -this study- or HYDRUS-1D - Er-Raki et al., 2021). These practical considerations also mean that even if the physical models are sound, real-world irrigation patterns may not align with hydrologically optimal strategies. Moreover, while we used deep percolation as a proxy for aquifer recharge, not all water draining below the root zone necessarily reaches the groundwater table. In this semi-arid environment, water may be stored or move laterally in the unsaturated zone, or even re-evaporate downstream. These processes are further complicated by the clayey soils that can slow vertical movement and by the highly variable groundwater depths in the Haouz-Mejjate aquifer region (30 to 260 m). Thus, the relationship between percolation at 90 cm and actual aquifer recharge can vary dramatically from plot to plot. Finally, this hydrological perspective on irrigation efficiency does not consider crop yield in itself or energy consumption through groundwater pumping which is larger for flood irrigation given the larger irrigation amounts.

This underscores that a society-relevant, precise assessment of irrigation systems efficiency here requires more integrative model-data approaches combining more field data on percolation with the strengths of process-based ecohydrological models like EcH_2O and HYDRUS-1D and hydrogeological components quantifying not only aquifer recharge but also the dynamics of groundwater pumping in realistic farming contexts.

5. Conclusions

By comparing a flood- with a drip-irrigated plot, this model-data study notably focuses on the resulting percolation beneath the root zone as a proxy for aquifer recharge—an increasingly vital understanding for sustainable water management in agriculture. The multi-criteria calibration and evaluation comparing various calibration scenarios overall showed that the ecohydrological model used in this study was able to capture hydrological and surface-atmosphere exchange dynamics with specific patterns inherent to each type of irrigation practice, and validated our first hypothesis that the complementary information content brought by soil water content, energy balance and percolation datasets warrants their joint use for improved model performance. However, our results reject our second hypothesis that drip irrigation enhances irrigation efficiency at all levels: when considering both transpiration and deep percolation as indices for useful water -the first as a proxy for biomass production, the second for recharging the underlying aquifer sustaining irrigation input, we find that flood irrigation is more efficient from a whole "aquifer-soil system" perspective.

These insights thus directly relate to questions which remain central for agriculture and policy development aiming at optimising the use of scarce water resources in farming environments. These encouraging results highlight the value of coupling a process-based description of the energy balance and hydrology, even if the latter is simplified, to simulate groundwater recharge rates in ET-dominated systems. It also points at the need for additional constraints to enhance our comprehension of the influence of site-specific characteristics on water movement and refining the corresponding estimates of recharge fluxes. One avenue is having longer or additional records of lysimeter-based percolation measurements across various soil types and irrigation systems, and (non exclusively) the integration of stable water isotopes monitoring with tracer-enabled ecohydrological models (Kuppel et al., 2018b). By tracking water movement both in quantity and in origin along the soil-plant-atmosphere continuum, such developments may better disentangle and predict the functional changes that low-latitude cultivated systems are undergoing (Scandellari et al., 2024) due to climatic and socio-economic trajectories. Coupling process-based models with transparent, basin-scale water accounts would thus allow informing on sustainable water management practices using an integrative assessment of irrigation efficiency at a variety of spatial and temporal scales; under current conditions and testing future scenario integrating water management policies and potential changes in cropping choices.

CRediT authorship contribution statement

Valérie Demarez: Writing – review & editing, Validation, Supervision, Formal analysis. **Abdelghani Chehbouni:** Supervision, Project administration, Funding acquisition. **ATTOU Taha:** Writing – review & editing, Writing – original draft, Visualization, Software, Methodology, Investigation, Formal analysis, Data curation, Conceptualization. **Sylvain Kuppel:** Writing – review & editing, Writing – original draft, Visualization, Validation, Supervision, Software, Methodology, Investigation, Formal analysis, Data curation, Conceptualization. **Mohamed Hakim Kharrou:** Writing – review & editing, Supervision, Project administration, Data curation. **Jamal Ezzahar:** Writing – review & editing, Visualization, Supervision, Data curation. **Lhoussaine Bouchaou:** Writing – review & editing, Validation, Supervision, Project administration. **Yassine Ait Brahim:** Writing – review & editing, Validation, Supervision.

Declaration of Competing Interest

The authors declare that they have no known competing financial interests or personal relationships that could have appeared to influence the work reported in this paper

Acknowledgements

The present work is financially supported by ASSIWAT project funded by the OCP Group S.A (Office Chérifien des Phosphates) (grant agreement no: AS_71) and the Horizon 2020 ACCWA project (grant agreement no: 823965) in the context of Marie Sklodowska-Curie research and the innovation staff exchange (RISE) program. We thank the Tensift Observatory and the TREMA International Joint Laboratory (https://www.lmi-trema.ma/) for the experimental set-up and providing us with the data of the study site. We would also like to thank the Moroccan Ministry of Higher Education, Scientific Research and Innovation and the OCP Foundation who supported this work through the APRD research program (GEANTech).

Appendix A. Supporting information

Supplementary data associated with this article can be found in the online version at doi:10.1016/j.agwat.2025.109584.

Data availability

Data will be made available on request.

References

Abou Ali, A., Bouchaou, L., Er-Raki, S., Hssaissoune, M., Brouziyne, Y., Ezzahar, J., Khabba, S., Chakir, A., Labbaci, A., Chehbouni, A., 2023. Assessment of crop evapotranspiration and deep percolation in a commercial irrigated citrus orchard under semiarid climate: Combined Eddy-Covariance measurement and soil water balance-based approach. Agric. Water Manag. 245, 107997. https://doi.org/10.1016/j.agwat.2022.107997.

Ackerer, J., Kuppel, S., Braud, I., Pasquet, S., Fovet, O., Probst, A., et al., 2023. Exploring the critical zone heterogeneity and the hydrological diversity using an integrated ecohydrological model in three contrasted long-term observatories. Water Resour. Res. 59, e2023WR035672. https://doi.org/10.1029/2023WR035672.

Akesbi, N., 2014. Which agricultural policy for which food security in Morocco?, in Seasonal Workers in Mediterranean Agriculture. Routledge, pp. 167–174. https://doi.org/10.4324/9781315884431-27.

Ala-Aho, P., Tetzlaff, D., McNamara, J.P., Laudon, H., Soulsby, C., 2017. Using isotopes to constrain water flux and age estimates in snow-influenced catchments using the STARR (Spatially distributed Tracer-Aided Rainfall–Runoff) model. Hydrol. Earth Syst. Sci. 21 (10), 5089–5110.

Arjdal, K., Vignon, É., Driouech, F., Chéruy, F., Er-Raki, S., Sima, A., Chehbouni, A., Drobinski, P., 2024. Modeling land–atmosphere interactions over semiarid plains in morocco: in-depth assessment of GCM stretched-grid simulations using in situ data. J. Appl. Meteorol. Climatol. 63 (3), 369–386. https://doi.org/10.1175/JAMC-D-23-0099.1.

Bao, C., Li, L., Shi, Y., Duffy, C., 2017. Understanding watershed hydrogeochemistry: 1. Development of RT-Flux-PIHM. Water Resour. Res. 53, 2328–2345. https://doi.org/10.1002/2016WR018934.

Benouniche, M., Kuper, M., Hammani, A., Boesveld, H., 2014. Making the user visible: analyzing irrigation practices and farmers' logic to explain actual drip irrigation performance. Irrig. Sci. https://doi.org/10.1007/s00271-014-0438-0.

Beven, K., 2006. A manifesto for the equifinality thesis. J. Hydrol. (Amst.) 320 (1–2), 18–36. https://doi.org/10.1016/J.JHYDROL.2005.07.007.

Birkel, C., Soulsby, C., Tetzlaff, D., 2014. Developing a consistent process-based conceptualization of catchment functioning using measurements of internal state variables. Water Resour. Res. 50 (4), 3481–3501. https://doi.org/10.1002/2013WR014925.

Bouchaou, L., Michelot, J.L., Vengosh, A., Hsissou, Y., Qurtobi, M., Gaye, C.B., Bullen, T.D., Zuppi, G.M., 2008. Application of multiple isotopic and geochemical tracers for investigation of recharge, salinization, and residence time of water in the Souss–Massa aquifer, southwest of Morocco. J. Hydrol. 352 (3–4), 267–287. https://doi.org/10.1016/j.jhydrol.2008.01.022.

Boukhari, K., Fakir, Y., Stigter, T.Y., Hajhouji, Y., Boulet, G., 2015. Origin of recharge and salinity and their role on management issues of a large alluvial aquifer system in the semi-arid Haouz plain, Morocco. Environ. Earth Sci. 73, 6195–6212. https://doi.org/10.1007/s12665-014-3844-y.

Cai, X., Zhang, X., Noël, P.H., Shafiee-Jood, M., 2015. Impacts of climate change on agricultural water management: a review. WIREs Water 2 (5), 439–455. https://doi.org/10.1002/wat2.1089.

Cao, W., Bowden, W.B., Davie, T., Fenemor, A., 2006. Multi-variable and multi-site calibration and validation of SWAT in a large mountainous catchment with high spatial variability. Hydrol. Process. 20 (5), 1057–1073. https://doi.org/10.1002/HYP.5933.

Chehbouni, A., Escadafal, R., Duchemin, B., Boulet, G., Simonneaux, V., Dedieu, G., Mougenot, B., Khabba, S., Kharrou, H., Maisongrande, P., Merlin, O., Chaponnière, A., Ezzahar, J., Er-Raki, S., Hoedjes, J., Hadria, R., Abourida, A., Cheggour, A., Raibi, F., Boudhar, A., Benhadj, I., Hanich, L., Benkaddour, A., Guemouria, N., Chehbouni, A.H., Lahrouni, A., Olioso, A., Jacob, F., Williams, D.G., Sobrino, J.A., 2008. An integrated modelling and remote sensing approach for hydrological study in arid and semi-arid regions: the SUDMED Programme. Int. J. Remote Sens. 29, 5161–5181. https://doi.org/10.1080/01431160802036417.

Clapp, R.B., Hornberger, G.M., 1978. Empirical equations for some soil hydraulic properties. Water Resour. Res. 14 (4), 601–604. https://doi.org/10.1029/WR014i004p00601.

Clark, M.P., Vrugt, J.A., 2006. Unraveling uncertainties in hydrologic model calibration: addressing the problem of compensatory parameters. Geophys. Res. Lett. 33 (6), L06406. https://doi.org/10.1029/2005GL025604.

Clark, M.P., Kavetski, D., Fenicia, F., 2011. Pursuing the method of multiple working hypotheses for hydrological modeling. Water Resour. Res. 47, W09301. https://doi.org/10.1029/2010WR009827.

Douinot, A., Tetzlaff, D., Maneta, M., Kuppel, S., Schulte-Bisping, H., Soulsby, C., 2019. Ecohydrological modelling with EcH$_2$O-iso to quantify forest and grassland effects on water partitioning and flux ages. Hydrol. Process. 33, 2174–2191. https://doi.org/10.1002/hyp.13480.

Efstratiadis, A., Koutsoyiannis, D., 2010. One decade of multi-objective calibration approaches in hydrological modelling: a review. Hydrol. Sci. J. 55, 58e78. https://doi.org/10.1080/02626660903526292.

El Mezouary, L., Hadri, A., Kharrou, M.H., Fakır, Y., Elfarchouni, A., Bouchaou, L., Chehbouni, A.-, 2024. Contribution to advancing aquifer geometric mapping using machine learning and deep learning techniques: a case study of the AL Haouz-Mejjate aquifer, Marrakech, Morocco. Appl. Water Sci. 14, 102. https://doi.org/10.1007/s13201-024-02162-x.

Er-Raki, S., Chehbouni, A., Boulet, G., Williams, D.G., 2010. Using the dual approach of FAO-56 for partitioning ET into soil and plant components for olive orchards in a semi-arid region. Agric. Water Manag. 97 (11), 1769–1778. https://doi.org/10.1016/j.agwat.2010.06.009.

Er-Raki, S., Ezzahar, J., Merlin, O., Amazirh, A., Hssaine, B.A., Kharrou, M.H., Khabba, S., Chehbouni, A., 2021. Performance of the HYDRUS-1D model for water balance components assessment of irrigated winter wheat under different water management in semi-arid regions of Morocco. Agric. Water Manag. 244, 106546. https://doi.org/10.1016/j.agwat.2020.106546.

Ez-zaouy, Y., Bouchaou, L., Saad, A., Hssaisoune, M., Brouziyne, Y., Dhiba, D., Chehbouni, A., 2022. Morocco's coastal aquifers: recent observations, evolution and perspectives towards sustainability. Environ. Pollut. 293, 118498. https://doi.org/10.1016/j.envpol.2021.118498.

Fatichi, S., Ivanov, V.Y., Caporali, E., 2012. A mechanistic ecohydrological model to investigate complex interactions in cold and warm water-controlled environments: 1. Theoretical framework and plot-scale analysis. J. Adv. Model. Earth Syst. 4 (2). https://doi.org/10.1029/2011MS000086.

Fatichi, S., Vivoni, E.R., Ogden, F.L., Ivanov, V.Y., Mirus, B., Gochis, D., Downer, C.W., Camporese, M., Davison, J.H., Ebel, B., et al., 2016. An overview of current applications, challenges, and future trends in distributed process-based models in hydrology. J. Hydrol. 537, 45e60. https://doi.org/10.1016/j.jhydrol.2016.03.026.

Fenicia, F., McDonnell, J.J., Savenije, H.H.G., 2008. Learning from model improvement: on the contribution of complementary data to process understanding. Water Resour. Res. 44 (6), W06419. https://doi.org/10.1029/2007WR006386.

Global Yield Cap Atlas, 2022. Morocco. https://www.yieldgap.org/Morocco.

Grafton, R.Q., Williams, J., Perry, C.J., Molle, F., Ringler, C., Steduto, P., Allen, R.G., 2018. The paradox of irrigation efficiency. Science 361 (6404), 748–750. https://doi.org/10.1126/science.aat9314.

Guo, J., Zheng, L., Ma, J., Li, X., Chen, R., 2023. Meta-analysis of the effect of subsurface irrigation on crop yield and water productivity. Sustainability 15 (22), 15716. https://doi.org/10.3390/su152215716.

Gupta, H.V., Kling, H., Yilmaz, K.K., Martinez, G.F., 2009. Decomposition of the mean squared error and NSE performance criteria: implications for improving hydrological modelling. J. Hydrol. 377, 80–91. https://doi.org/10.1016/j.jhydrol.2009.08.003.

Hargrove, W.L., Heyman, J.M., Mayer, A., Mirchi, A., Granados-Olivas, A., Ganjegunte, G., Gutzler, D., Pennington, D.D., Ward, F.A., Chavira, L.G., Sheng, Z., Kumar, S., Villanueva-Rosales, N., Walker, W.S., 2023. The future of water in a desert river basin facing climate change and competing demands: a holistic approach to water sustainability in arid and semi-arid regions. J. Hydrol.: Reg. Stud. 46, 101336. https://doi.org/10.1016/j.ejrh.2023.101336.

Ivanov, V.Y., Bras, R.L., Vivoni, E.R., 2008. Vegetation-hydrology dynamics in complex terrain of semiarid areas: 1. A mechanistic approach to modeling dynamic feedbacks. Water Resour. Res. 44 (3). https://doi.org/10.1029/2006WR005588.

Jasechko, S., Birks, S.J., Gleeson, T., Wada, Y., Fawcett, P.J., Sharp, Z.D., McDonnell, J. J., Welker, J.M., 2014. The pronounced seasonality of global groundwater recharge. Water Resour. Res. 50, 8845–8867. https://doi.org/10.1002/2014WR015809.

Jounaid, H., Attou, T., Remmal, T., Bouaziz, A., 2020. Securing access to drinking water in North-Eastern Morocco: the example of the taourirt-oujda corridor. Water 12 (4), 928. https://doi.org/10.3390/w12040928.

Kharrou, M.H., Simonneaux, V., Er-Raki, S., Le Page, M., Khabba, S., Chehbouni, A., 2021. Assessing irrigation water use with remote sensing-based soil water balance at an irrigation scheme level in a semi-arid region of Morocco. Remote Sens. 13 (6), 1133. https://doi.org/10.3390/rs13061133.

Knoben, W.J.M., Freer, J.E., Woods, R.A., 2019. Technical note: inherent benchmark or not? Comparing Nash–Sutcliffe and Kling–Gupta efficiency scores. Hydrol. Earth Syst. Sci. 23, 4323–4331. https://doi.org/10.5194/hess-23-4323-2019.

Krause, P., Boyle, D.P., Bäse, F., 2005. Comparison of different efficiency criteria for hydrological model assessment. Adv. Geosci. 5, 89–97. https://doi.org/10.5194/adgeo-5-89-2005.

Kuffour, B.N.O., Engdahl, N.B., Woodward, C.S., Condon, L.E., Kollet, S., Maxwell, R.M., 2020. Simulating coupled surface–subsurface flows with ParFlow v3.5.0: capabilities, applications, and ongoing development of an open-source, massively parallel, integrated hydrologic model. Geosci. Model Dev. 13, 1373–1397. https://doi.org/10.5194/gmd-13-1373-2020.

Kundzewicz, Z.W., 2008. Climate change impacts on the hydrological cycle. Ecohydrol. Hydrobiol. 8 (2–4), 195–203. https://doi.org/10.2478/v10104-009-0015-y.

Kuppel, S., Tetzlaff, D., Maneta, M.P., Soulsby, C., 2018a. What can we learn from multi-data calibration of a process-based ecohydrological model? Environ. Model. Softw. 101, 301–316. https://doi.org/10.1016/j.envsoft.2018.01.001.

Kuppel, S., Tetzlaff, D., Maneta, M.P., Soulsby, C., 2018b. EcH$_2$O-iso 1.0: water isotopes and age tracking in a process-based, distributed ecohydrological model. Geosci. Model Dev. 11, 3045–3069. https://doi.org/10.5194/gmd-11-3045-2018.

Le Page, M., Berjamy, B., Fakir, Y., Bourgin, F., Jarlan, L., Abourida, A., Benrhanem, M., Jacob, G., Huber, M., Sghrer, F., Simonneaux, V., Chehbouni, G., 2012. An integrated DSS for groundwater management based on remote sensing. the case of a semi-arid aquifer in Morocco. Water Resour. Manag. 26, 3209–3230. https://doi.org/10.1007/s11269-012-0068-3.

Li, K., Kuppel, S., Knighton, J., 2023. Parameterizing vegetation traits with a process-based ecohydrological model and xylem water isotopic observations. J. Adv. Model. Earth Syst. 15, e2022MS003263. https://doi.org/10.1029/2022MS003263.

Lozano-Parra, J., Maneta, M.P., Schnabel, S., 2014. Climate and topographic controls on simulated pasture production in a semiarid Mediterranean watershed with scattered tree cover. Hydrol. Earth Syst. Sci. 18, 1439–1456. https://doi.org/10.5194/hess-18-1439-2014.

Luo, S., Tetzlaff, D., Smith, A., Soulsby, C., 2024. Long-term drought effects on landscape water storage and recovery under contrasting landuses. J. Hydrol. 636, 131339. https://doi.org/10.1016/j.jhydrol.2024.131339.

Ma, S., Wang, T., Ma, S., 2022. Effects of drip irrigation on root activity pattern, root-sourced signal characteristics and yield stability of winter wheat. Agric. Water Manag 271, 107783. https://doi.org/10.1016/j.agwat.2022.107783.

Maneta, M.P., Silverman, N.L., 2013. A spatially distributed model to simulate water, energy, and vegetation dynamics using information from regional climate models. Earth Interact. 17 (11), 1–44. https://doi.org/10.1175/2012EI000472.1.

Mansir, I., Bouchaou, L., Chebli, B., Ait Brahim, Y., Choukr-Allah, R., 2021. A specific indicator approach for the assessment of water resource vulnerability in arid areas: the case of the Souss-Massa Region (Morocco). Hydrol. Sci. J. 66 (7), 1151–1168. https://doi.org/10.1080/02626667.2021.1924379.

Mays, L.W., 2010. Water resources engineering, second ed. John Wiley & Sons, Hoboken.

McDermid, S., Nocco, M., Lawston-Parker, P., et al., 2023. Irrigation in the earth system. Nat. Rev. Earth Environ. 4, 435–453. https://doi.org/10.1038/s43017-023-00438-5.

McDonnell, J.J., Sivapalan, M., Vaché, K., Dunn, S., Grant, G., Haggerty, R., et al., 2007. Moving beyond heterogeneity and process complexity: a new vision for watershed hydrology. Water Resour. Res. 43 (7), W07301. https://doi.org/10.1029/2006WR005467.

Molle, F., Tanouti, O., 2017. Squaring the circle: agricultural intensification vs. water conservation in Morocco. Agric. Water Manag. 192, 170–179.

Morris, M.D., 1991. Factorial sampling plans for preliminary computational experiments. Technometrics 33 (2), 161. https://doi.org/10.2307/1269043.

Moukhchane, M., 1983. Contribution à l'étude des réservoirs aquifères profonds de la bordure Nord de l'Atlas, entre Demnate et Imin'Tanout (Maroc). Thèse Doctorat 3ème Cycle. Université De Franche-Comté, Fac. Scie., Tech.

Muñoz-Sabater, J., Dutra, E., Agustí-Panareda, A., Albergel, C., Arduini, G., Balsamo, G., Boussetta, S., Choulga, M., Harrigan, S., Hersbach, H., Martens, B., Miralles, D.G., Piles, M., Rodríguez-Fernández, N.J., Zsoter, E., Buontempo, C., Thépaut, J.-N., 2021. ERA5-Land: a state-of-the-art global reanalysis dataset for land applications. Earth Syst. Sci. Data 13 (9), 4349–4383. https://doi.org/10.5194/essd-13-4349-2021.

Neill, A.J., Birkel, C., Maneta, M.P., Tetzlaff, D., Soulsby, C., 2021. Structural changes to forests during regeneration affect water flux partitioning, water ages and hydrological connectivity: Insights from tracer-aided ecohydrological modelling. Hydrol. Earth Syst. Sci. 25, 4861–4886. https://doi.org/10.5194/hess-25-4861-2021.

Niu, G.-Y., Paniconi, C., Troch, P.A., Scott, R.L., Durcik, M., Zeng, X., Goodrich, D.C., 2014. An integrated modelling framework of catchment-scale ecohydrological processes: 1. Model description and tests over an energy-limited watershed. Ecohydrology 7, 427–439. https://doi.org/10.1002/eco.1362.

Or, D., Lehmann, P., Shahraeeni, E., Shokri, N., 2013. Advances in soil evaporation physics—a review. vzj2012.0163 Vadose Zone J. 12, 1–16. https://doi.org/10.2136/vzj2012.0163.

Ouarani, M., Brahim, Y.A., Mulla, D., Rafik, A., Azennoud, K., Bouchaou, L., Chehbouni, A., 2023. A comprehensive overview of groundwater salinization and recharge processes in a semi-arid coastal aquifer (Essaouira, Morocco). J. Hydrol.: Reg. Stud. 49, 101501. https://doi.org/10.1016/j.ejrh.2023.101501.

Ouassanouan, Y., Fakir, Y., Simonneaux, V., Kharrou, M.H., Bouimouass, H., Najar, I., Benrhanem, M., Sguir, F., Chehbouni, A., 2022. Multi-decadal analysis of water resources and agricultural change in a Mediterranean semiarid irrigated piedmont under water scarcity and human interaction. Sci. Total Environ. 834, 155328. https://doi.org/10.1016/j.scitotenv.2022.155328.

Ourrai, S., Aithssaine, B., Amazirh, A., Er-Raki, S., Bouchaou, L., Jacob, F., Chehbouni, A., 2024. Assessment of the modified two-source energy balance (TSEB) model for estimating evapotranspiration and its components over an irrigated olive orchard in Morocco. Agric. Water Manag. 298. https://doi.org/10.1016/j.agwat.2024.108861.

Piovano, T.I., Tetzlaff, D., Ala-aho, P., Buttle, J., Mitchell, C.P.J., Soulsby, C., 2018. Testing a spatially distributed tracer-aided runoff model in a snow-influenced catchment: Effects of multicriteria calibration on streamwater ages. Hydrol. Process. 32 (20), 3089–3107. https://doi.org/10.1002/HYP.13238.

Pueyo, Y., Moret-Fernández, D., Saiz, H., Bueno, C.G., Alados, C.L., 2013. Relationships Between Plant Spatial Patterns, Water Infiltration Capacity, and Plant Community Composition in Semi-arid Mediterranean Ecosystems Along Stress Gradients. Ecosystems 16 (3), 452–466. https://doi.org/10.1007/s10021-012-9620-5.

Scandellari, F., Attou, T., Barbeta, A., Bernhard, F., D'Amato, C., Dimitrova-Petrova, K., Sprenger, M., 2024. Using stable isotopes to inform water resource management in forested and agricultural ecosystems. J. Environ. Manag. 365, 121381. https://doi.org/10.1016/j.jenvman.2024.121381.

Scudeler, C., Pangle, L., Pasetto, D., Niu, G.-Y., Volkmann, T., Paniconi, C., et al., 2016. Multiresponse modeling of variably saturated flow and isotope tracer transport for a hillslope experiment at the Landscape Evolution Observatory. Hydrol. Earth Syst. Sci. 20 (10), 4061–4078. https://doi.org/10.5194/hess-20-4061-2016.

Seibert, J., McDonnell, J.J., 2002. On the dialog between experimentalist and modeler in catchment hydrology: Use of soft data for multicriteria model calibration. Water Resour. Res. 38 (11), 23-1–23-14. https://doi.org/10.1029/2001WR000978.

Šimůnek, J., Šejna, M., Saito, H., Sakai, M., and van Genuchten, M.T. (2008). The HYDRUS-1D software package for simulating the movement of water, heat, and multiple solutes in variably-saturated media. University of California Riverside Research Reports, 3.

Sohier, H., Farges, J.-L., Piet-Lahanier, H., 2014. Improvement of the representativity of the morris method for air-launch-to-orbit separation. IFAC Proc. Vol. 47 (3), 7954–7959. https://doi.org/10.3182/20140824-6-ZA-1003.01968.

Tague, C.L., Band, L.E., 2004. RHESSys: regional hydro-ecologic simulation system—An object-oriented approach to spatially distributed modeling of carbon, water, and nutrient cycling. Earth Interact. 8 (19), 1–42. https://doi.org/10.1175/1087-3562(2004)8%3C1:RRHSSO%3E2.0.CO;2.

Toumi, J., Er-Raki, S., Ezzahar, J., Khabba, S., Jarlan, L., Chehbouni, A., 2016. Performance assessment of AquaCrop model for estimating evapotranspiration, soil water content and grain yield of winter wheat in Tensift Al Haouz (Morocco): application to irrigation management. Agric. Water Manag. 163 (1), 219–235. https://doi.org/10.1016/j.agwat.2015.09.007.

Twine, T.E., Kustas, W.P., Norman, J.M., Cook, D.R., Houser, P.R., Meyers, T.P., Prueger, J.H., Starks, P.J., Wesely, M.L., 2000. Correcting eddy-covariance flux underestimates over a grassland. Agric. For. Meteorol. 103 (3), 279–300. https://doi.org/10.1016/s0168-1923(00)00123-4.

Ward, F.A., Pulido-Velazquez, M., 2008. Water conservation in irrigation can increase water use. Proc. Natl. Acad. Sci. U. S. A. 105 (47), 18215–18220. https://doi.org/10.1073/pnas.0805554105.

World Bank, 2020. Morocco Green Generation Program-for-Results Project. World Bank. Retrieved from. 〈https://documents1.worldbank.org/curated/en/245801608346893390/pdf/Morocco-Green-Generation-Program-for-Results-Project.pdf〉.

Wythers, K.R., Lauenroth, W.K., Paruelo, J.M., 1999. "Bare-soil evaporation under semiarid field conditions. Soil Sci. Soc. Am. J. 63 (5), 1341–1349. https://doi.org/10.2136/sssaj1999.6351341x.

Yang, X., Tetzlaff, D., Soulsby, C., Smith, A., Borchardt, D., 2021. Catchment functioning under prolonged drought stress: tracer-aided ecohydrological modeling in an intensively managed agricultural catchment. Water Resour. Res. 57, e2020WR029094. https://doi.org/10.1029/2020WR029094.

Yang, X., Tetzlaff, D., Müller, C., Knöller, K., Borchardt, D., Soulsby, C., 2023. Upscaling tracer-aided ecohydrological modeling to larger catchments: Implications for process representation and heterogeneity in landscape organization. Water Resour. Res. 59, e2022WR033033. https://doi.org/10.1029/2022WR033033.